RESEARCH ARTICLE

Concentration Estimation for Fuel Cells: Design of Experiments, Nonlinear Identification, and Observer Design With Experimental Validation

ZHANG PENG DU[1], **CHRISTOPH STEINDL**[2], **STEFAN JAKUBEK**[1], **AND CHRISTOPH HAMETNER**[3]

[1]Institute of Mechanics and Mechatronics, TU Wien, 1060 Vienna, Austria
[2]Institute of Powertrains and Automotive Technology, TU Wien, 1060 Vienna, Austria
[3]Christian Doppler Laboratory for Innovative Control and Monitoring of Automotive Powertrain Systems, TU Wien, 1060 Vienna, Austria

Corresponding author: Zhang Peng Du (zhang.peng.du@tuwien.ac.at)

ABSTRACT Fuel cells (FCs) are promising eco-friendly power sources. Nevertheless, there are challenges to overcome if they are to be widely deployed in areas such as degradation avoidance and control, where the knowledge of the unavailable concentrations is crucial. In this respect, observers can provide unavailable quantities based on an estimation algorithm and available measurements. This paper presents an FC concentration observer design workflow, covering the model-based design of experiments (DOE), their execution, systematic nonlinear identification, and measurement-based validation. The model-based DOE and the validation with a mass spectrometer, including dynamic operation, are unique for PEMFC observers. The workflow is demonstrated with a constrained extended Kalman filter observer on a 30 kW polymer electrolyte membrane FC (PEMFC) test stand. A control-oriented model serves as the workflow basis, and the DOE is based on optimizing the parameter sensitivity. The test stand delivers the measurements, the parametrization comprises a sensitivity analysis, and the experimentally validated observer yields outstanding concentration estimation performance.

INDEX TERMS Design of experiments, design workflow, experimental validation, fuel cells, Kalman filter, mass spectrometer, observer, parameter sensitivity analysis, parametrization, PEMFC.

I. INTRODUCTION

Polymer electrolyte membrane fuel cells (PEMFCs) are a promising, environmentally friendly mobile power source suitable for widespread use. The reasons for this are their relatively high fuel efficiencies, low operating temperatures, and comparatively simple constructions. However, the market share for fuel cells (FCs) remains minimal on account of several challenges. Among these challenges is the fact that PEMFCs are still relatively expensive because production volumes are low. Moreover, FCs are prone to degradation

due to improper operation, and they are not simple to control because of their complex internal processes [1]. Observers would go some way to overcoming these challenges. This paper describes a novel holistic design workflow for PEMFC concentration observers covering the design of experiments (DOE), their execution, nonlinear model identification, and experimental validation.

What are observers?

Observers estimate unmeasured or even unmeasurable quantities based on measured ones and an estimation algorithm. Quantities of interest are, e.g., FC concentrations, humidities, and state of health. Thus, they represent a meaningful way to lower costs by reducing the number of physical

---

The associate editor coordinating the review of this manuscript and approving it for publication was Zhiwei Gao.

sensors, minimizing degradation through online diagnostics, and providing the essential foundation for model-based control.

What types of observers exist?

Observers are a model-based diagnosis method in addition to non-model-based methods such as neural networks or statistical methods. Model-based methods can be further subdivided into lumped (only time dependency) or distributed parameters (time and location dependency) and linear or nonlinear. Both distinctions hold for observers and models [2]. This paper focuses on observers based on models, which are nonlinear with lumped parameters, to exploit advantages in combination with model-based controllers [3]. Lumped parameter FC observers can be roughly categorized in two ways: One way is by the underlying estimation algorithm type [2]: Kalman filter [4], Luenberger [5], sliding mode [6], [7], adaptive [8], and other observers [9], [10], [11]. Another way of categorizing is by the desired estimated quantity, e.g., gas concentrations [12], parameters [13], state of health [14], and faults [15].

What is the state-of-the-art for observer design workflows?

An observer design workflow often only covers the design of an estimation algorithm and its validation and, in rare cases, parameter identification (see Table 1). They rely mainly on FC model parameters obtained from the literature or emulators, and few workflows used identified parameters from an experimental setup to replicate the behavior satisfactorily. Well-established and relatively static experiments, such as a polarization curve or current steps, are usually used for identification and validation. The validation of a concentration observer is executed mainly in a simulation environment, and experimental validations are rare due to the lack of required hardware but are indispensable for real-world applications. If at all, only single concentrations are experimentally validated with relatively static experiments.

What is the knowledge gap?

To the best of the authors' knowledge, target-oriented DOE for observer design considering the underlying system characteristics is a novelty, and a design workflow including a measurement-based parametrization is not common practice (see Table 1). In particular, no experimental observer validation of PEMFC concentrations during transient operations currently exists. In conclusion, no paper thus far covers a holistic observer design workflow starting from the DOE through the systematic nonlinear parameter identification to the experimental validation of PEMFC concentration observers.

How does this paper close the knowledge gap?

This paper presents such a holistic design workflow for PEMFC concentration observers. The workflow with a given model consists of three steps: First, a model-based DOE is performed utilizing the parameter sensitivities (Fisher information). Second, the designed experiments are conducted on a 30 kW PEMFC system test stand with a mass spectrometer.

TABLE 1. Comparison of observer design workflows.

Reference	Design of experiment	Parametrization	Validation
[4], [10]	Steps	Literature	Simulation
[5]	Fault scenarios	Experimental	Simulation
[6]	Vehicle test standard	Literature	Simulation
[7]	Steps	Given	Simulation
[8]	Polarization curve	Experimental	Experimental (resistance)
[9]	Steps	Given	PEMFC emulator
[11], [15]	Fault scenarios	Literature	Simulation
[12]	Steps	Experimental	Simulation
[13]	Steps	Experimental (Parameter observer)	Simulation
[14]	Existing measurements	Experimental	Experimental (voltage)
This work	Model-based	Experimental	Experimental (concentration)

A parameter sensitivity analysis assesses how well the model parameters can be estimated with the measured data, and the model is parameterized based on these results. The third and final step is the observer design, followed by validation with experimental data. The authors' study [16] describes a PEMFC model, which serves as the modeling basis because it can reproduce various effects of water, essential for degradation avoidance and diagnosis. The observer estimation algorithm used to demonstrate the design workflow is based on [4], a constrained extended Kalman filter (CEKF). This model-based observer for stochastic systems was chosen because it allows the exploitation of computational advantages related to the Jacobians with model-based controllers [17].

What is the contribution of this paper?

The main contribution of this paper is the holistic design workflow for FC concentration observers, covering the named three steps for the first time. Moreover, the model-based DOE and the experimental concentration validation with a mass spectrometer, including dynamic operations, are unique for PEMFC observers. A holistic workflow is beneficial as a guideline for real-world implementations. Especially in real cases with limited resources of time and budget, a dedicated DOE increases the experiment's parameter information content and excitation quality compared to non-specifically designed ones of the same length. Thus, shorter and fewer experiments are necessary to achieve sufficient parametrization and validation results. Systematic parametrization and experiments with high parameter information content simplify identification and are advantageous to obtaining an observer that replicates the real-world system satisfactorily. Lastly, a validation with actual state measurements is indispensable to approve the observer for real-world applications where outstanding concentration estimation results are achieved in this work.

The remainder of this paper is structured as follows: Section II presents the holistic observer design workflow with an overview of the PEMFC model and describes the experimental setup used. Section III shows the obtained results, followed by a detailed discussion.

II. METHODS AND EXPERIMENTAL SETUP

This section describes the novel holistic design workflow for PEMFC concentration observers, which combines three (partially) existing methods in a target-oriented way: model-based DOE, systematic nonlinear identification, and observer design with experimental validation. In addition, the model is briefly described, and one of this paper's key components is the mass spectrometer utilized to obtain the concentrations, which is part of the experimental setup introduced here. Note that this workflow is not limited to the presented model and observer.

A. MODEL-BASED DESIGN OF EXPERIMENTS

The underlying FC model for the concentration observer design workflow is introduced here, following which the model-based DOE is presented.

1) FUEL CELL MODEL

The modeling basis for our approach is a control-oriented lumped parameter PEMFC stack model as presented in [16] with the following assumptions: The respective manifolds are lumped into one volume with no spatial expansion. The gases are ideal and have homogeneous properties inside a manifold. The gas composition in the exit manifold is the same as in the center manifold, and the model has only one uniform and externally controlled temperature. The supply manifolds, the exit manifolds, and the gas diffusion layers are always in a steady-state condition, and dry air consists only of oxygen and nitrogen. An advantage of this model is the capability to reproduce various water effects in a physically motivated way, which is indispensable for online diagnoses and degradation avoidance. Furthermore, the model is analytically differentiable, which allows exact determination of the Jacobians for model-based observers and controllers. The model consists of four interconnected submodels: the cathode, anode, membrane, and electrochemical submodel, as shown in Fig. 1. The internal dynamics are modeled using thermodynamics, electrochemistry, and fluid mechanics. The supply and exit manifolds are connected via nozzle equations with the center manifold or the environment, and on the anode side, there is an additional recirculation flow path powered by a pump. The membrane connects the cathode and the anode, and these submodels deliver the electrochemical model's prerequisites. As in [16], the state-space representation for this nonlinear model is given as

$$\dot{x} = f(x, u, \theta), y = g(x, u, \theta), \quad (1)$$

and the respective vectors are structured as

$$x = [m_{\text{ca},O_2}, m_{\text{ca},N_2}, m_{\text{ca,vap}}, m_{\text{ca,liq}}, \ldots$$

$$\ldots m_{\text{an},H_2}, m_{\text{an},N_2}, m_{\text{an,vap}}, m_{\text{an,liq}}, a_m]^T, \quad (2a)$$

$$u = [\dot{m}_{\text{ca,in}}, \varphi_{\text{ca,in}}, \alpha_{\text{ca}}, I, T, p_{\text{atm}}, \ldots$$

$$\ldots p_{\text{an,sm}}, \varphi_{\text{an,in}}, \alpha_{\text{an}}, P_{\text{an,reci}}]^T, \quad (2b)$$

$$y = [U, p_{\text{ca,sm}}, p_{\text{ca,em}}, \dot{m}_{\text{an,in}}, p_{\text{an,em}}]^T, \quad (2c)$$

$$\theta = [V_{\text{ca}}, V_{\text{an}}, k_{\text{phase}}, k_{\text{liq}}, \ldots$$

$$\ldots k_{\text{ca,cm,sm}}, k_{\text{ca,em,cm}}, k_{\text{ca,atm,em}}, \ldots$$

$$\ldots k_{\text{an,cm,sm}}, k_{\text{an,em,cm}}, k_{\text{an,atm,em}}, \tau_m, \ldots$$

$$\ldots R_c, K_{\text{ca}}, K_{\text{an}}, D_{\text{ca}}, D_{\text{an}}]^T. \quad (2d)$$

Here, $x \in \mathbb{R}^9$ is the state vector, $u \in \mathbb{R}^{10}$ the input vector, $y \in \mathbb{R}^5$ the output vector, $\theta \in \mathbb{R}^{16}$ the vector containing the tunable parameters, f the system function, and g the output function [18]. The state $x = x(t)$, input $u = u(t)$, and output vector $y = y(t)$ are time-dependent, whereas the parameter vector θ is constant. The states consist mainly of the gas and liquid water masses on the cathode and anode sides, denoted by m. The subscripts indicate cathode (ca), anode (an), oxygen (O_2), hydrogen (H_2), nitrogen (N_2), water vapor (vap), and liquid water (liq). The last state is the membrane water activity a_m. Observing these states is essential to avoid fuel starvation, membrane dehydration, and flooding effects. The inputs on the cathode side are the incoming airflow $\dot{m}_{\text{ca,in}}$, the airflow relative humidity $\varphi_{\text{ca,in}}$, and the backpressure valve position α_{ca}. Additional model inputs are the stack current I, the uniform stack temperature T, and the atmosphere pressure p_{atm}. On the anode side, the inputs are the supply manifold pressure $p_{\text{an,sm}}$, the relative humidity of the incoming flow $\varphi_{\text{an,in}}$, the purge valve position α_{an}, and the recirculation pump power $P_{\text{an,reci}}$. The model outputs are the stack voltage U, the cathode supply $p_{\text{ca,sm}}$ and exit manifold pressure $p_{\text{ca,em}}$, and the anode inflowing mass $\dot{m}_{\text{an,in}}$ and exit manifold pressure $p_{\text{an,em}}$. The tunable parameters of the model are the respective volumes V, various mass flow and nozzle coefficients k, the characteristic membrane time constant τ_m, the ohmic contact resistance R_c, the intrinsic exchange current parameters K, and the combined diffusivities D. The derivation of model equations is beyond the scope of this paper, and the reader is referred to [16] in this regard.

2) DESIGN OF EXPERIMENTS

Experiment execution can be reduced to a minimum by a purposeful DOE to increase the parameter information content. By doing so, the experiments deliver better parametrization results and yield a more profound validation by exploiting the fully available actuator range compared to non-specifically designed ones of the same length. FC concentration measurements, in particular, are costly and complex, so reducing the number and length is of economic interest. Apart from the cost, established experiments such as a polarization curve or current steps do not use the whole actuator range, e.g., temperatures and stoichiometries are kept constant, which is a limitation for identification and validation.

The parameter information content utilized in our approach is the so-called Fisher information matrix (FIM) M [19]. This
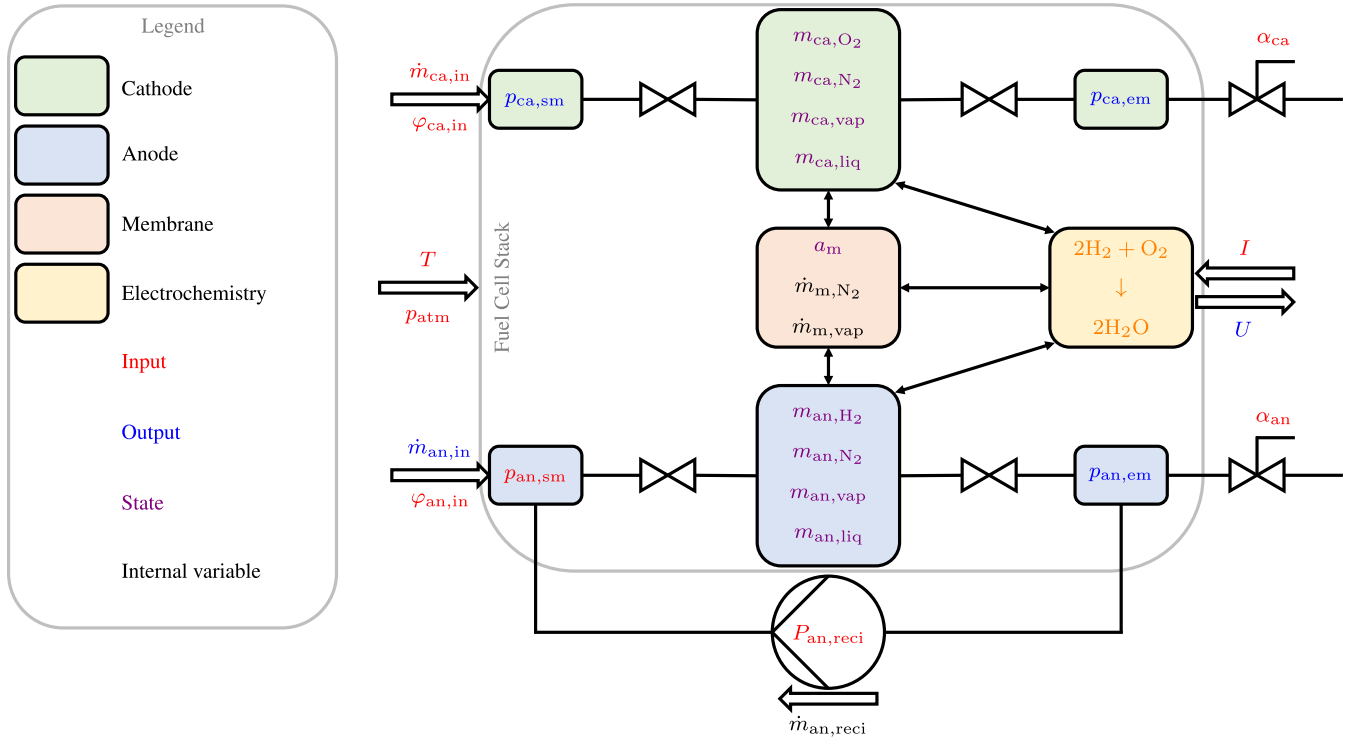
FIGURE 1. Schematic overview of PEMFC stack model structure [16].

is beneficial because according to the Cramér–Rao inequality as in [19] and [20],

$$\text{Cov}(\boldsymbol{\theta}) \succeq \boldsymbol{M}^{-1}, \tag{3}$$

the inverse of $\boldsymbol{M}$ is the lower bound of the parameter covariance matrix $\text{Cov}(\boldsymbol{\theta})$. Thus, increasing the FIM lowers the parameter uncertainty and improves the parametrization result of the FC model. In order to calculate it, first, the state parameter sensitivity $\boldsymbol{\xi}_i = \text{d}\boldsymbol{x}/\text{d}\theta_i$, is needed, where θ_i for $i \in \{1, 2, \ldots, n_\theta\}$ denotes a tunable parameter, and n_θ is the number of parameters. As in [19] and [21], $\boldsymbol{\xi}_i$ is obtained by solving the following first-order ordinary differential equation, which is a total derivative of the FC model (1):

$$\begin{aligned}
\dot{\boldsymbol{\xi}}_i &= \frac{\text{d}}{\text{d}t}\left(\frac{\text{d}\boldsymbol{x}}{\text{d}\theta_i}\right) = \frac{\text{d}}{\text{d}\theta_i}\left(\frac{\text{d}\boldsymbol{x}}{\text{d}t}\right) = \frac{\text{d}}{\text{d}\theta_i}\boldsymbol{f}(\boldsymbol{x}, \boldsymbol{u}, \boldsymbol{\theta}) \\
&= \frac{\partial \boldsymbol{f}(\boldsymbol{x}, \boldsymbol{u}, \boldsymbol{\theta})}{\partial \boldsymbol{x}}\frac{\text{d}\boldsymbol{x}}{\text{d}\theta_i} + \frac{\partial \boldsymbol{f}(\boldsymbol{x}, \boldsymbol{u}, \boldsymbol{\theta})}{\partial \theta_i} \\
&= \frac{\partial \boldsymbol{f}(\boldsymbol{x}, \boldsymbol{u}, \boldsymbol{\theta})}{\partial \boldsymbol{x}}\boldsymbol{\xi}_i + \frac{\partial \boldsymbol{f}(\boldsymbol{x}, \boldsymbol{u}, \boldsymbol{\theta})}{\partial \theta_i}. \tag{4}
\end{aligned}$$

Second, the output parameter sensitivity $\boldsymbol{\psi}_i = \text{d}\boldsymbol{y}/\text{d}\theta_i$ is evaluated using $\boldsymbol{\xi}_i$ as in [21]:

$$\begin{aligned}
\boldsymbol{\psi}_i &= \frac{\partial \boldsymbol{g}(\boldsymbol{x}, \boldsymbol{u}, \boldsymbol{\theta})}{\partial \boldsymbol{x}}\frac{\text{d}\boldsymbol{x}}{\text{d}\theta_i} + \frac{\partial \boldsymbol{g}(\boldsymbol{x}, \boldsymbol{u}, \boldsymbol{\theta})}{\partial \theta_i} \\
&= \frac{\partial \boldsymbol{g}(\boldsymbol{x}, \boldsymbol{u}, \boldsymbol{\theta})}{\partial \boldsymbol{x}}\boldsymbol{\xi}_i + \frac{\partial \boldsymbol{g}(\boldsymbol{x}, \boldsymbol{u}, \boldsymbol{\theta})}{\partial \theta_i}. \tag{5}
\end{aligned}$$

Within the scope of the DOE, the output vector $\boldsymbol{y}$ is extended with the respective cathode $x_{\text{ca},p}$ for $p \in$

$\{O_2, N_2, \text{vap}\}$ and anode gaseous species mole fractions $x_{\text{an},p}$ for $p \in \{H_2, N_2, \text{vap}\}$ to exploit the additional parameter information provided by the mass spectrometer measurements. The output parameter sensitivity matrix $\boldsymbol{\Psi}(t) = \left[\boldsymbol{\psi}_1(t), \boldsymbol{\psi}_2(t), \ldots, \boldsymbol{\psi}_{n_\theta}(t)\right]$ is obtained by stacking every $\boldsymbol{\psi}_i$ for each parameter θ_i into one matrix. Sampling it at time instants k, $\boldsymbol{M}$ is finally computed as in [21] with

$$\boldsymbol{M} = \sum_{k=0}^{n_k} \boldsymbol{\Psi}_k^{\text{T}}\boldsymbol{\Sigma}_e^{-1}\boldsymbol{\Psi}_k. \tag{6}$$

Here, $\boldsymbol{\Sigma}_e$ represents the prediction error covariance matrix, which is the measurement noise covariance under the assumption of a perfect model, and $\boldsymbol{M} \in \mathbb{R}^{n_\theta \times n_\theta}$ holds.

As shown by the FIM derivation, it is highly nonlinear, and an analytical solution for an optimal $\boldsymbol{M}$ is exceptionally complicated to find. Thus, to simplify this evaluation, the FIM is heuristically tuned for an optimized steady-state input $\boldsymbol{u}_{\text{opt},i}$ for each parameter θ_i independently. Note that in the case of a single parameter, the FIM reduces to a scalar M_i, resulting in n_θ optimized steady-state operating points for every parameter θ_i. For the given parameters (2), this corresponds to 16 operating points. These are pieced together into one long experiment, where each operating point $\boldsymbol{u}_{\text{opt},i}$ is held for some time and represents an optimized point to identify the respective parameter θ_i in steady-state. The optimization problem is formulated as follows:

$$\boldsymbol{u}_{\text{opt},i} = \arg\min_{\boldsymbol{u}} \frac{1}{M_i(\boldsymbol{u})} \text{ for } i \in \{1, 2, \ldots, n_\theta\}$$

with respect to

$$\dot{x} = f(x, u, \theta) = 0$$

$$u_{l,\min} \leq u_l \leq u_{l,\max} \text{ for } l \in \{1, 2, \ldots, n_u\}. \quad (7)$$

The optimization requires a first guess of the parameters θ_i based on literature values and expert knowledge. Subsequently, a heuristic optimizer [22] chooses an input candidate subject to the constraints with the minimum $u_{l,\min}$ and maximum value $u_{l,\max}$ of each input component u_l (n_u is the total number of input components). It is important to bear in mind that only the following inputs are actively and (almost) independently controllable: the incoming airflow $\dot{m}_{ca,in}$, stack current I, inflowing coolant temperature (assumed to be the stack temperature T within the scope of the optimization), and anode supply manifold pressure $p_{an,sm}$. The remaining inputs are either not controllable (disturbances), dependent on the actively controlled inputs, or constant. Model (1) is simulated with this constant input u until it reaches steady-state $\dot{x} = 0$, and finally, M_i is calculated based on a single steady-state instant ($n_k = 0$). Analogously to the Cramér–Rao inequality (3), the inverse of M_i constitutes the objective function. After the optimizer delivers a result, the proceeding is repeated for the remaining parameters. Time constant-like parameters are poorly estimable during (quasi) steady-state, so an additional dynamic experiment should be conducted. The excitation during this experiment could be a sine signal covering the whole amplitude and frequency operating range (chirp or sweep signal [23]).

B. MEASUREMENT-BASED AND SYSTEMATIC NONLINEAR IDENTIFICATION

In order to conduct the systematic nonlinear identification with measurement data, the designed experiments have to be executed, and the desired signals, including concentrations, need to be measured on the PEMFC experimental setup. This section describes the experimental setup, followed by an overview of the systematic nonlinear identification approach.

1) EXPERIMENTAL SETUP

The measurements for the parametrization and validation within the observer design workflow are obtained using a commercial 30 kW PEMFC stack. This stack is operated on a dedicated test stand, equipped with the associated balance-of-plant components and a specifically designed control system. The schematic overview of the system test stand is highlighted in Fig. 2, and further information on this can be found in [21]. The paper describes in detail the main subsystems of air supply, hydrogen supply, thermal management, and measurement and control, together with all technical specifications of the FC stack and auxiliary subsystems.

Based on the specifically developed control system to execute the highly dynamic and demanding experiments and the various implemented sensors to measure the required quantities for the design workflow (e.g., pressure, temperature, humidity, current, and voltage), the operation and operating behavior of a PEMFC system can be analyzed and assessed in detail. Within the scope of the design workflow, the following system inputs could be adjusted independently:

- Air mass flow,
- Hydrogen supply pressure, and
- FC coolant inlet temperature.

Also, the load point of the FC stack can be controlled either by setting the stack voltage or the stack current with the dynamic DC/AC inverter (battery simulator). The latter is used for all experiments in our research.

A feature of our approach is the use of an additional measurement device to obtain information about the inner states of the FC stack, i.e., the gas compositions at the cathode or anode side, which are generally unmeasured in most investigations. The continuously measured FC gas concentrations during dynamic experiments are essential for measurement-based identification, experimental observer validation, and diagnostic purposes. Therefore, an electron impact ionization mass spectrometer (PEMSense, V&F Analyse- und Messtechnik GmbH [24]) is integrated on the test stand. This mass spectrometer can rapidly analyze gas species with a mass range of 1-100 amu, sufficient to measure all relevant components like H_2, N_2, O_2, H_2O, and CO_2 in a PEMFC. The measurable gas concentrations start from 100 ppm and reach up to 100 vol% (mol% is equivalent to vol% assuming ideal gas) depending on the species and can be measured with an accuracy of $\pm 3\%$. The mass spectrometer is equipped with two separate sample gas inlets to analyze gas probes, one at the anode and another at the cathode side, with the restriction that only one sample gas line can be analyzed at a time. Fig. 2 shows that the probe extraction positions at the anode side are directly at the outlet of the water separator and at the cathode side after the exhaust manifold of the FC stack. Only the sample gas line at the anode side is used for the experiments in our research due to limited resources. For this reason, all the following statements refer to the gas analysis of the anode side. Continuous gas extraction allows a real-time analysis with a response time smaller than two seconds. Also, only a small amount of gas mass is sampled compared to the consumed hydrogen of the FC stack. It is therefore guaranteed that the gas extraction does not influence the operation and the operating behavior of the FC stack. Generally, the gas is sampled with a heated capillary to mitigate a condensation of the gaseous species during gas analysis. Thus, it is not possible to differentiate between the gaseous and the liquid phase of the species of interest. Another restriction comes with the fact that, as mentioned earlier, the gas extraction position is at the outlet of the water separator. As a result, only the partially dehumidified anode exhaust gas is measured. Moreover, due to the drift of the concentrations related to the mass spectrometer over time (up to $\pm 5\%$ over 24 h), a calibration of the device using test gases of all relevant gas species is conducted at the beginning of every day of the measurement study. Calibration gases with the concerned species with an accuracy of the concentration of $\pm 2\%$ are
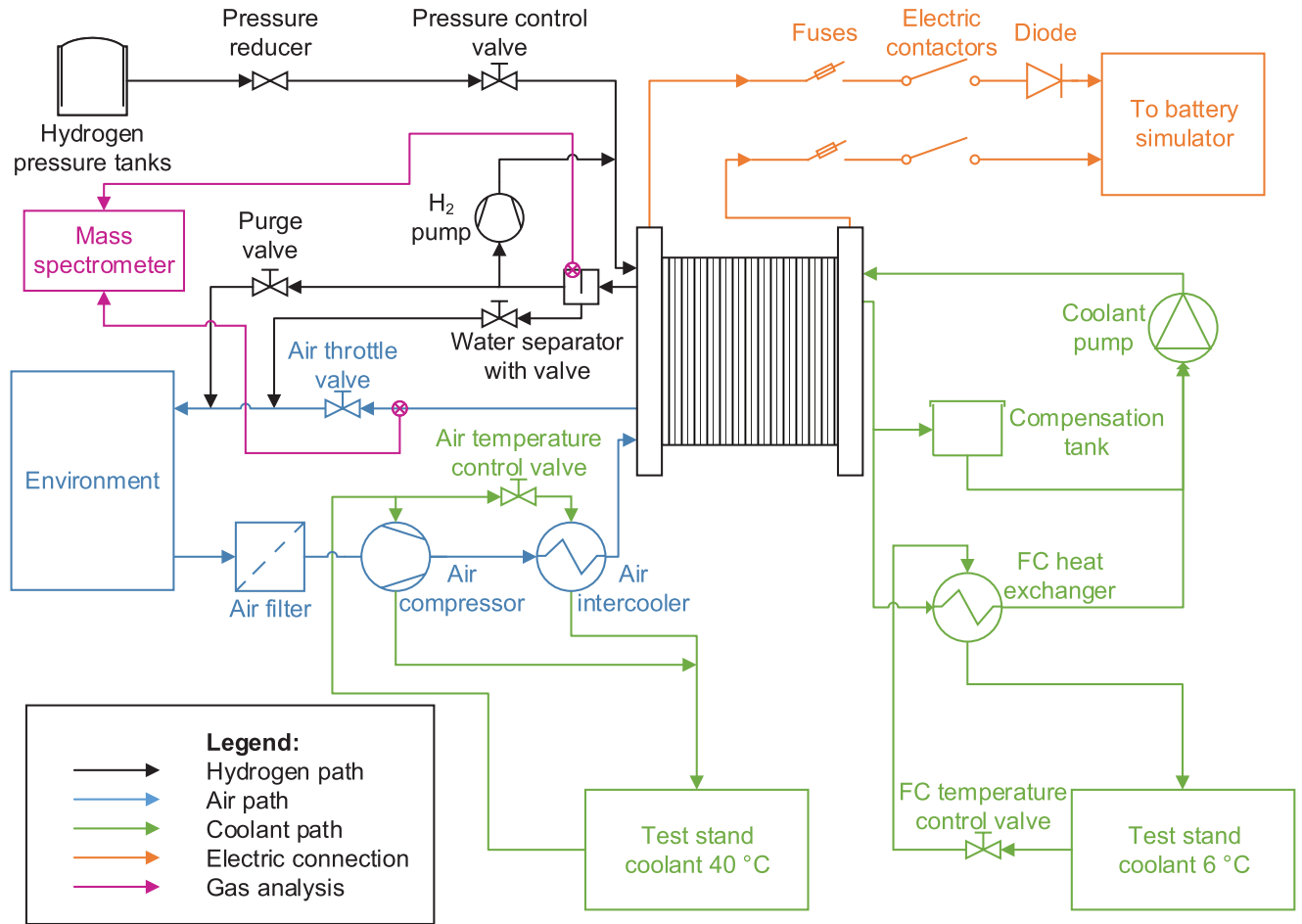
FIGURE 2. Schematic FC system test stand setup.

used. The acquisition of measurement data from the mass spectrometer is realized with a sampling rate of 3 Hz.

Seven measurement series were carried out for parameterization and validation of the observer, considering reproducibility. The following measurement series are available: one polarization curve experiment, three specifically designed experiments for parameter identification, and three dynamic experiments with a chirp signal as load demand. The experiments are detailed in Section III, where simulated and measured results are presented and discussed.

2) SYSTEMATIC NONLINEAR IDENTIFICATION

The sensitivity analysis of the FC model's parameters excludes poorly identifiable parameters and simplifies the parametrization problem. E.g., the manifold volumes V behave like a time constant and are thus better identifiable during transient operation, though the experiment barely contains any transients. Another striking example is modeling-related, e.g., two parameters are linearly dependent, which means both can not be uniquely identified. The FIM M is utilized for this analysis and is evaluated analogously to Section II-A2 for sample instants n_k, measured inputs u^*, and all tunable FC parameters θ_i simultaneously. The parameter

values vary by many orders of magnitude, e.g., the ohmic contact resistance R_c has the magnitude 10^0, and the nozzle coefficients k 10^{-6}. This requires a normalized FIM M_{nrm}, as in [25] and [26], to evaluate the parameter identifiability meaningfully:

$$M_{nrm} = \text{diag}(\theta) M \text{diag}(\theta). \tag{8}$$

Here, $\text{diag}(\theta)$ represents a matrix with the elements of θ in its main diagonal. This normalization is unnecessary for the DOE because only one parameter at a time is considered there. As in [27], [28], a singular value decomposition is applied to M_{nrm} to evaluate the parameter significances:

$$M_{nrm} = USV^T. \tag{9}$$

In the singular value decomposition, U is the matrix comprising the left singular vectors, $V = [v_1, v_2, \ldots, v_{n_\theta}]$ the right singular vectors, and $S = \text{diag}(\sigma_1, \sigma_2, \ldots, \sigma_{n_\theta})$ is the diagonal singular value matrix. A singular value σ_j for $j \in \{1, 2, \ldots, n_\theta\}$ can be understood as the amount of parameter information, and the associated singular vector shows the parameter space direction of this information. E.g., a high singular value mainly pointing in the direction of a nozzle

coefficient k means that the parameter has high information, is uniquely identifiable, and significantly influences the model output. The right singular vectors $\boldsymbol{v}_j \in \mathbb{R}^{n_\theta}$ are utilized to evaluate the parameter significances, and the Euclidean norm from each is 1. From this it can be concluded that the relative direction share of a vector component $v_{j,i}$ is $v_{j,i}^2$ [29]. The singular value σ_j multiplied with the proper relative direction share yields the amount of information of that specific singular value pointing in the parameter θ_i's direction. Therefore, the sum of the information shares of every singular value pointing in one parameter θ_i's direction, as in [21], delivers the parameter's total information σ_{θ_i}:

$$\sigma_{\theta_i} = \sum_{j=1}^{n_\theta} \sigma_j v_{j,i}^2. \tag{10}$$

Based on each σ_{θ_i} magnitude, a subset of the parameters with the highest information content is chosen for parametrization and is denoted as the most significant parameters $\boldsymbol{\theta}_{ms}$. They are selected by arranging the σ_{θ_i} in descending order, and only the first $n_{\boldsymbol{\theta}_{ms}}$ most significant parameters are considered until the inequality, as in [21], holds:

$$\frac{\sum_{i=1}^{n_{\boldsymbol{\theta}_{ms}}} \sigma_{\theta_{ms,i}}}{\sum_{i=1}^{n_{\boldsymbol{\theta}}} \sigma_{\theta_i}} \geq \gamma \tag{11}$$

The threshold $\gamma \in [0, 1]$ is adaptable for different purposes, and $n_{\boldsymbol{\theta}_{ms}} \leq n_{\boldsymbol{\theta}}$ holds. Due to their minimal information content, the least significant and not considered parameters are negligible for the model output or are unidentifiable using the given model and available experiments. Interestingly, optimizing the real-world counterpart of a most significant parameter influences the measurable system output more significantly than optimizing a barely significant one.

In order to obtain a parametrized model (1) to replicate the real PEMFC satisfactorily, an objective function J is defined. As in [21], [30], it comprises the $(n_k + 1)$ weighted squared errors between the simulated $\boldsymbol{y}(t_k, \boldsymbol{\theta})$ and measured outputs $\boldsymbol{y}_k^*$, and a regularization term:

$$J(\boldsymbol{\theta}) = \sum_{k=0}^{n_k} \left(\boldsymbol{y}(t_k, \boldsymbol{\theta}) - \boldsymbol{y}_k^*\right)^{\mathrm{T}} \boldsymbol{Q}_{\boldsymbol{y}} \left(\boldsymbol{y}(t_k, \boldsymbol{\theta}) - \boldsymbol{y}_k^*\right) + \ldots$$
$$\ldots (\boldsymbol{\theta}_0 - \boldsymbol{\theta})^{\mathrm{T}} \boldsymbol{Q}_{\boldsymbol{\theta}} (\boldsymbol{\theta}_0 - \boldsymbol{\theta}). \tag{12}$$

The t_k corresponds to the time of the sample instant k, and in the objective function, $\boldsymbol{Q}_{\boldsymbol{y}}$ represents the output weighting matrix to weigh the individual outputs and consider the different output magnitudes, e.g., the anode inflowing mass $\dot{m}_{an,in}$ has a magnitude of 10^{-4} and the pressures p 10^5, which would lead to a bias in the parametrization. Moreover, $\boldsymbol{\theta}_0$ is a realistic initial guess of the parameters, and $\boldsymbol{Q}_{\boldsymbol{\theta}}$ is the regularization matrix to penalize the deviation of the parameter vector $\boldsymbol{\theta}$ from its initial value $\boldsymbol{\theta}_0$ in consideration of the different parameter magnitudes. The regularization also considers different parameter uncertainty levels, e.g., volumes V only vary in a narrow range due to little manufacturing tolerances. However, the combined diffusivities D vary

by many orders of magnitude because very little is known. As in [21], the following optimization problem yields the optimized parameters $\boldsymbol{\theta}_{opt}$:

$$\boldsymbol{\theta}_{opt} = \arg \min_{\boldsymbol{\theta}} J(\boldsymbol{\theta})$$
$$\text{with respect to}$$
$$\theta_{i,min} \leq \theta_i \leq \theta_{i,max} \text{ for } i \in \{1, 2, \ldots, n_\theta\}. \tag{13}$$

The parameter space needs to be constrained to simplify the optimization and obtain meaningful results. The constraints are obtained from expert knowledge and physical considerations [21], e.g., the bounds for the volumes V can be derived from geometrical information, and all the parameters θ_i are strictly positive. Within the scope of parametrization, the model outputs are extended with the measured FC concentrations from the mass spectrometer to exploit its additional available parameter information, and the least significant parameters are kept constant. If multiple experiments are considered simultaneously in the optimization, the summation of the squared errors is extended over all experiments, and additional error weighting depending on the specific experiment can be considered.

C. OBSERVER DESIGN WITH EXPERIMENTAL VALIDATION

Finally, the design of the concentration observer based on the CEKF estimation algorithm is presented, followed by a description of the experimental validation approach used.

1) CONSTRAINED EXTENDED KALMAN FILTER

Knowing the FC concentrations is essential for degradation avoidance, diagnosis, and control. However, they are usually unmeasured, so observers come into play, estimating the unmeasured or even unmeasurable quantities based on an estimation algorithm and measured signals. The underlying observer estimation algorithm within the workflow is a CEKF based on [4]. The choice fell on the model-based observer for stochastic systems because the necessary Jacobians can be directly reused for model-based controllers [3], [17], saving computational resources. The applied observer is adapted to the given FC model (1), and solving the latter yields time-continuous signals, e.g., $\boldsymbol{x}$. However, digital observers and controllers process the time-discrete counterpart, e.g., $\boldsymbol{x}_k$, obtained by sampling $\boldsymbol{x}$ at time instants $k \in \{0, 1, \ldots, n_k\}$, where $(n_k + 1)$ is the total number of samples and assuming zero-order hold. Thus, according to [4], the time-discrete equivalent of model (1) considering noise is

$$\boldsymbol{x}_k = \boldsymbol{F}(\boldsymbol{x}_{k-1}, \boldsymbol{u}_{k-1}, \boldsymbol{\theta}), \boldsymbol{y}_k = \boldsymbol{g}(\boldsymbol{x}_k, \boldsymbol{u}_k, \boldsymbol{\theta}), \tag{14a}$$
$$\boldsymbol{x}_k^* = \boldsymbol{x}_k + \boldsymbol{w}_{\boldsymbol{x},k-1}, \boldsymbol{y}_k^* = \boldsymbol{y}_k + \boldsymbol{w}_{\boldsymbol{y},k}. \tag{14b}$$

Here, $\boldsymbol{F}(\boldsymbol{x}_{k-1}, \boldsymbol{u}_{k-1}, \boldsymbol{\theta})$ is the discrete system prediction function, and it predicts the state $\boldsymbol{x}_k$ at instant k by solving (1) over a sampling period using quantities from the previous instant. The unchanged output function $\boldsymbol{g}$ is not affected by discretization because it is a mapping function and not a differential equation. Adding process noise $\boldsymbol{w}_{\boldsymbol{x}}$ and measurement

noise w_y to the state x and output y yield the starred noisy (and measured) analogs, respectively. In line with [4], it is assumed that the noises are white and uncorrelated, and their covariances are known:

$$w_x \sim \mathcal{N}(0, \Sigma_x), w_y \sim \mathcal{N}(0, \Sigma_y),$$
$$x_0 \sim \mathcal{N}(\bar{x}_0, \Sigma_{x_0}). \quad (15)$$

Here, $\mathcal{N}$ denotes normal distribution with the mean value as the first argument and the covariance as the second. Thus, the process w_x and measurement noise w_y are normally distributed and have zero mean with known covariances Σ_x and Σ_y, respectively. The initial state x_0, which needs to be estimated, has a mean of $\bar{x}_0$ and a known covariance of Σ_{x_0}. For the respective covariances, $\Sigma \succ 0$ holds. In practice, x_0 can be estimated up to a certain degree of accuracy by taking the first sample of the measured FC signals and applying fundamental relations, e.g., assuming humid air and calculating the concentrations within the cathode. The estimation algorithm is separated into a prediction and an update step. As in [4], the state $\hat{x}_k^-$ and covariance estimate $\hat{\Sigma}_{\hat{x},k}^-$ are predicted using past quantities:

$$\hat{x}_k^- = F(\hat{x}_{k-1}, u_{k-1}, \theta), \quad (16a)$$
$$\hat{\Sigma}_{\hat{x},k}^- = A_{k-1} \hat{\Sigma}_{\hat{x},k-1} A_{k-1}^T + \Sigma_x. \quad (16b)$$

The superscripted minus indicates prediction, and the initial conditions are $\hat{x}_0 = x_0$ and $\hat{\Sigma}_{\hat{x},0} = \Sigma_{x_0}$. The discretized system matrix A_{k-1} is a partial derivative of model (1), elaborated on later. The output estimate is predicted with $\hat{y}_k^- = g(\hat{x}_k^-, u_k, \theta)$. The update step consists of three equations, utilizing current quantities and exploiting the current measured output y_k^*. Following [4], the optimal Kalman gain L_k is evaluated first, which is necessary to obtain the updated state $\hat{x}_k$ and covariance estimate $\hat{\Sigma}_{\hat{x},k}$:

$$L_k = \overbrace{\hat{\Sigma}_{\hat{x},k}^- C_k^T}^{K_k} \overbrace{(C_k \hat{\Sigma}_{\hat{x},k}^- C_k^T + \Sigma_y)^{-1}}^{H_k}, \quad (17a)$$
$$\hat{x}_k = \hat{x}_k^- + L_k(y_k^* - \hat{y}_k^-), \quad (17b)$$
$$\hat{\Sigma}_{\hat{x},k} = (I - L_k C_k)\hat{\Sigma}_{\hat{x},k}^-(I - L_k C_k)^T + \dots$$
$$\dots L_k \Sigma_y L_k^T. \quad (17c)$$

The output matrix C_k is a partial model derivative, I is an identity matrix, and K_k and H_k simplify the notation. The updated state estimate $\hat{x}_k$ is subject to inequality constraints $\hat{x}_{k,m} \geq x_{\lim,m}$ for $m \in \{1, 2, \dots, n_x\}$, where $x_{\lim}$ contains the state limit values, and n_x is the number of states. The constraint is necessary because the unconstrained algorithm does not guarantee estimated states within a physically plausible range. If no state constraint is violated, the algorithm is finished at instant k. Otherwise, the gain projection method is utilized to obtain an adjusted optimal Kalman gain $\tilde{L}_k$ to fulfill the constraints. The clipped state estimate $\tilde{x}_k$ is used, which is equal to $\hat{x}_k$, except that the elements that do not comply with the constraints are clipped to the limit value.

As in [4], the adjusted Kalman gain is obtained with

$$\begin{bmatrix} \tilde{L}_k, \Lambda \end{bmatrix} \begin{bmatrix} K_k, (\tilde{x}_k - \hat{x}_k^-) \end{bmatrix} \cdot \dots$$
$$\dots \begin{bmatrix} H_k & (y_k^* - \hat{y}_k^-) \\ (y_k^* - \hat{y}_k^-)^T & 0 \end{bmatrix}^{-1}, \quad (18)$$

where Λ is the Lagrangian multiplier vector. The state and covariance estimate update (17) is repeated with $\tilde{L}_k$ to obtain the constrained counterpart. Finally, the updated output estimate is evaluated from $\hat{y}_k = g(\hat{x}_k, u_k, \theta)$, and the algorithm is executed every instant to observe the desired quantities continuously. The required Jacobians are analytically derived from the nonlinear FC model (1), as in [4]:

$$A(t_{k-1}) = \left. \frac{\partial f(x, u, \theta)}{\partial x} \right|_{\hat{x}_{k-1}, u_{k-1}, \theta}$$
$$C(t_k) = \left. \frac{\partial g(x, u, \theta)}{\partial x} \right|_{\hat{x}_k^-, u_k, \theta} \quad (19)$$

which are also necessary for model-based controllers. The model derivatives are calculated using a toolbox [31], and the time-continuous $A(t_{k-1})$ needs to be discretized accordingly to get the time-discrete counterpart A_{k-1}. For the discretization procedure and further details, please refer to [4].

2) EXPERIMENTAL VALIDATION
In the final step, the observer is validated with separate validation data sets. In order to do this, only the measured inputs u^* and outputs y^* are fed into the observer, while it estimates the states $\hat{x}$. The measured ones x^* are entirely unknown to it. This configuration enables the observer to run parallel to a test stand or other real-world applications. For validation, it is shown that the observer estimates the measured FC concentrations well without knowing the actual measured quantities and that it replicates the concentrations better than an open-loop simulation of the model alone. As in [32], the scatter index $S \in [0, \infty)$, also known as normalized root-mean-square error, is used to evaluate the goodness of replicating the measured signal y^* by the estimated (or simulated) counterpart $\hat{y}$, defined as

$$S = \frac{\sqrt{\frac{1}{n_k+1} \sum_{k=0}^{n_k} \left(y_k^* - \hat{y}_k\right)^2}}{\frac{1}{n_k+1} \sum_{k=0}^{n_k} y_k^*}. \quad (20)$$

Here, the nominator represents the root-mean-square error between the measured and the estimated (simulated) signal, and the denominator is the arithmetic mean of the measured signal. An S value of 0 means perfect replicating of the measurements by the model or observer, and increasing values imply progressively worse performance.

III. RESULTS AND DISCUSSION
This section presents the results of the model-based DOE. These are conducted on the experimental setup, and the resulting measurements are shown. The nonlinear identification is conducted based on the measurements, and the resulting replication performance of the model is illustrated.

The observer is experimentally validated based on the concentration measurements, and the superior performance of the observer compared to an open-loop model simulation is demonstrated. In addition, all the results are discussed in detail.

A. DESIGNED EXPERIMENTS

The DOE optimization (7) is conducted considering that only the following inputs are actively and (almost) independently controllable: the incoming airflow $\dot{m}_{ca,in}$, stack current I, inflowing coolant temperature (assumed to be the stack temperature T), and anode supply manifold pressure $p_{an,sm}$. The gaseous species x are additionally considered as outputs within the scope of optimization to exploit the additional parameter information content provided by the mass spectrometer signals. The optimized steady-state points are shown in Fig. 3a-d, and as additional information, the stoichiometry of air λ_{ca} is given in Fig. 3e.

Model (1) has 16 parameters, so there are 16 sections, each representing an optimized steady-state operating point to identify one specific parameter. The experiment starts and ends from the same point, and the steady-state points were arranged so that the change from one to the next is minimal due to control reasons. Please note that the given actuator ranges (red dashed lines) are well exploited, e.g., the entire temperature range (Fig. 3d) and various air stoichiometries (Fig. 3e) are used, which are often kept constant in polarization curve experiments. The stoichiometry is slightly above the given limit at the beginning and end due to the mitigation of cell flooding. Otherwise, the flow velocities on the cathode side at low current densities are too low to remove the produced water sufficiently. The results are plausible because, e.g., the water phase change coefficient k_{phase} ($t \in [1100\,s, 1200\,s]$) is well identifiable during low stack temperatures and little incoming airflow (Fig. 3a), leading to high relative humidities. The liquid water removal coefficient k_{liq} ($t \in [700\,s, 800\,s]$) is better identifiable during low temperatures and high currents (Fig. 3c), leading to many droplets being dragged out by a high incoming airflow. Interestingly, as shown in Fig. 3b, it is more advantageous regarding parameter identifiability to have the anode supply manifold pressure in the lower operating range. One reason could be that a lower pressure leads to less diffusion through the membrane, favoring the identification of nozzle coefficients (e.g., $k_{ca,cm,sm}$ and $k_{ca,em,cm}$ for $t \in [1300\,s, 1500\,s]$) because of lower disturbance flows. An additional chirp experiment (Fig. 3f) is executed to excite the parameter information of time constant-like parameters. The dynamic experiment utilizes the entire allowed current operating range and frequency while the remaining actuators are kept constant or are dependent on the current. The covered frequency starts from 0 Hz and rises to 0.06 Hz, limited by a given rate of change of $10\,A\,s^{-1}$. The steady-state point optimization objective value (7) for each parameter versus generation is shown in Fig. 3g, where the objective values are normed so that the first generation has the value 1. It can be seen that the objectives

only improve a little over the generations, the reason being that a used heuristic optimizer [22] population of 48 is rather large for four constrained decision variables. Thus, the initial solution is already good, leading to minimal changes over the generations. This information could be used for future optimizations, e.g., reducing the population size to reduce the computation time.

B. EXPERIMENTAL RESULTS

The optimized steady-state points, chirp, and polarization curve experiments are conducted (multiple times) on the experimental setup. The polarization curve experiment serves as a reference for further evaluations. Due to technical restrictions, either the cathode or the anode gaseous mole fractions can be measured during an experiment. Because of limited resources and theoretical higher information content according to the FIM, only the anode mole fractions are measured in all the experiments. One of the measurement cycles of each experiment is chosen, and the corresponding outputs, actively controllable inputs, air stoichiometry, and the anode gaseous mole fractions are shown in Fig. 4.

The left column represents the optimized steady-state points, the middle the chirp, and the right the polarization curve experiment. Blue indicates a system output, and red is an actively controllable input or air stoichiometry. The top first row (Fig. 4a-c) shows the stack voltage U and current I. In principle, all three experiments cover the entire operating range regarding input excitation, but only the chirp sweeps through the entire frequency range. The same conclusion holds for the second row (Fig. 4d-f), where the cathode supply manifold pressure $p_{ca,sm}$ and incoming airflow $\dot{m}_{ca,in}$ are shown. The third row illustrates the cathode exit manifold pressure $p_{ca,em}$ and air stoichiometry λ_{ca}. Interestingly, the steady-state points (Fig. 4g) and chirp experiment (Fig. 4h) cover the whole given air stoichiometry range, where a constant value (1.5) is tracked in the polarization curve one (Fig. 4i) for currents over 90 A (to avoid cell flooding), and higher stoichiometries are tracked during lower currents. In the steady-state points experiment, the air stoichiometry briefly exceeds the given bounds (peaks are outside the figure at about $t = \{220\,s, 920\,s\}$) due to quick load changes. The anode inflowing mass $\dot{m}_{an,in}$ and supply manifold pressure $p_{an,sm}$ are depicted in the fourth row. What is notable here is that $p_{an,sm}$ is essentially held constant in the chirp (Fig. 4k) and polarization curve experiment (Fig. 4l), and for the steady-state points experiment (Fig. 4j), it is actively varied. The fifth row (Fig. 4m-o) depicts the anode exit manifold pressure $p_{an,em}$ and outflowing coolant temperature (assumed to be the uniform stack temperature T). The not shown inflowing coolant temperature is almost constant for the chirp and polarization curve experiment, and the resulting temperature changes in the outgoing flow result mainly from the internal electrochemical reactions of the FC, explaining the correlation with the electric load. Again, the inflowing coolant temperature is actively varied only in the steady-state points experiment. The last row (Fig. 4p-r)

Design of Experiment
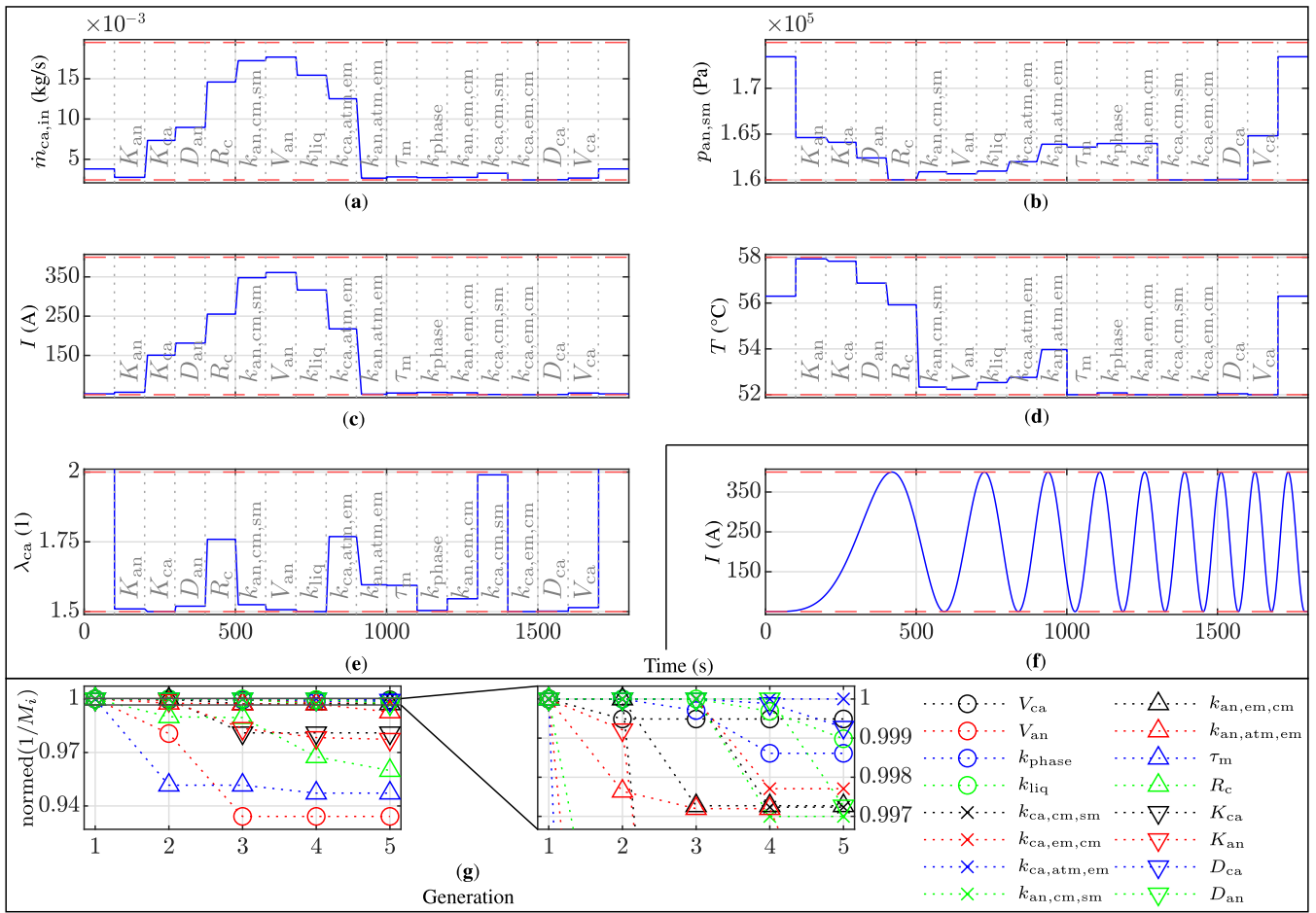
FIGURE 3. Plots (a-d) show the actively and (almost) independently controllable inputs for the designed steady-state points experiment: (a) incoming airflow $\dot{m}_{ca,in}$, (b) anode supply manifold pressure $p_{an,sm}$, (c) stack current I, and (d) the stack temperature T. The air stoichiometry λ_{ca} is given in (e) as additional information, and each section in (a-e) corresponds to an optimized steady-state operating point to identify one specific parameter, which is also given in grey. Plot (f) illustrates the additional chirp experiment, and the red dashed lines indicate the given actuator limits. Plot (g) shows each parameter's normed steady-state point optimization objective value versus generation.

displays the gaseous anode species mole fractions $x_{an,p}$ of hydrogen, nitrogen, and vapor. The experiments have similar mole fraction magnitudes quantitatively, but the trajectories deviate qualitatively mainly because of the applied loads. The spikes in the fourth- and fifth-row anode signals and the sharp jumps in the species mole fractions are due to anode purgings triggered by a Coulomb counter.

C. PARAMETRIZED MODEL

Well-established experiments, e.g., polarization curve or current steps, provide a reasonable basis for identification and are thus usually used for this purpose. Within the scope of our study, we investigated whether a purposefully designed experiment would yield any improvements regarding parametrization. Hence, it is shown here that the designed steady-state points experiment (Fig. 4 left column) yields better parameter identifiability than the polarization curve experiment (right column), and following this, the actual model parametrization results are presented. The polarization

curve experiment is longer in time, which generally suggests more parameter information, so only the same length as the steady-state points experiment starting from the beginning is taken to be a fair comparison.

The total parameter information σ_{θ_i} (10) is given in Fig. 5a. The red crosses denote the information content of the respective parameters based on the optimized steady-state points experiment, and the blue circles are the counterparts of the polarization curve experiment. Higher values indicate lower uncertainties in estimating the respective parameters with the particular experiment. In direct comparison, both experiments yield similar parameter information magnitudes. Thus, a definitive conclusion regarding better parameter identifiability of a specific experiment cannot yet be made, and note that the Fisher information is an a priori variance estimate. The parameters are estimated 134 times in total by solving the optimization problem (13) with a heuristic optimizer [22], where each run is independently and randomly initialized to obtain the sample for the empirical variance calculation.
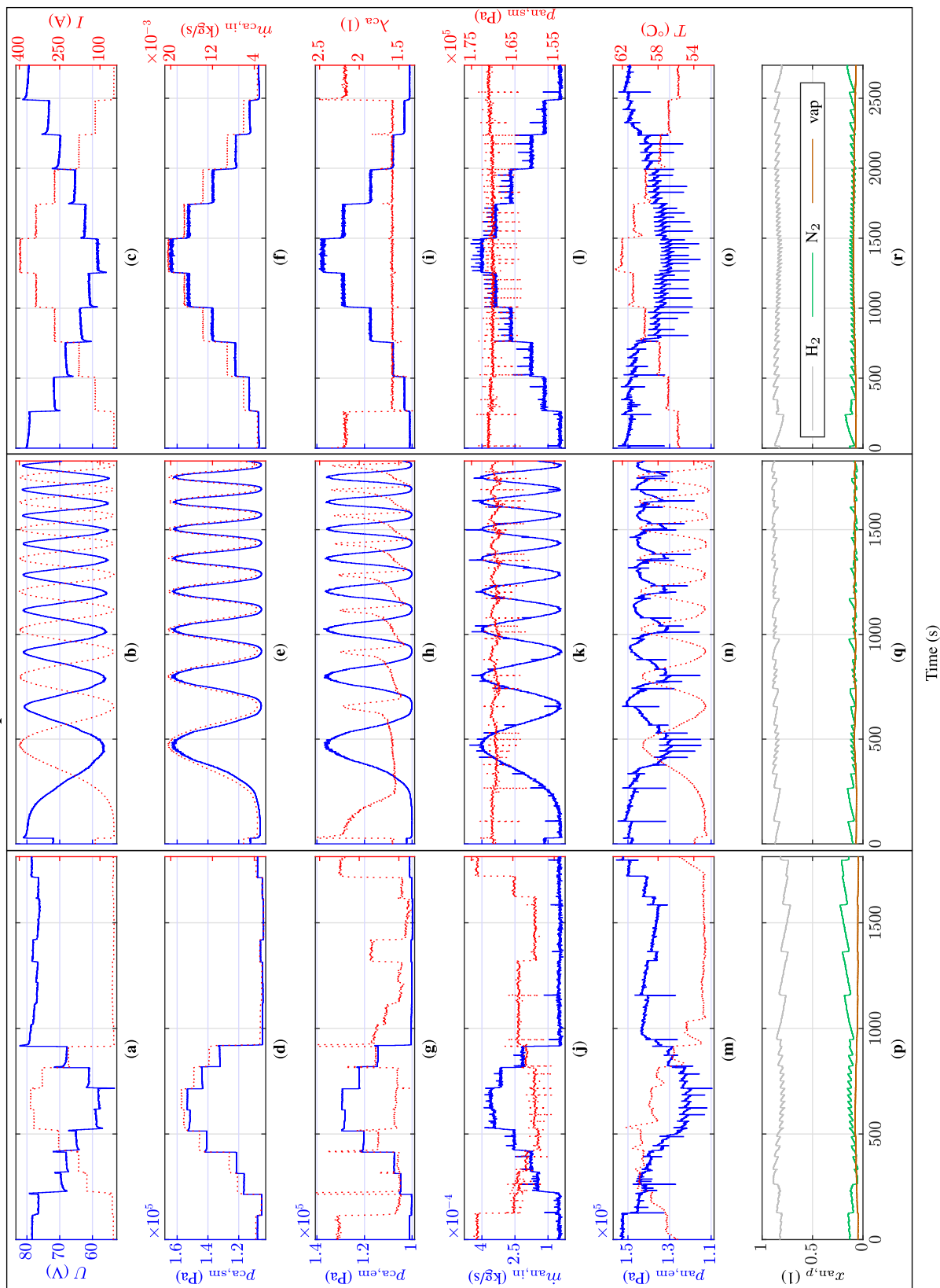
FIGURE 4. The left column shows the optimized steady-state points, the middle the chirp, and the right the polarization curve experiment. Blue indicates system output, and red is an actively controllable input or air stoichiometry. Plots (a-c) show the stack voltage U and current I, (d-f) cathode supply manifold pressure $p_{ca,sm}$ and incoming airflow $\dot{m}_{ca,in}$, and (g-i) cathode exit manifold pressure $p_{ca,em}$ and air stoichiometry λ_{ca}. Plots (j-l) represent the anode inflowing mass $\dot{m}_{an,in}$ and anode supply manifold pressure $p_{an,sm}$, (m-o) the anode exit manifold pressure $p_{an,em}$ and stack temperature T, and (p-r) the gaseous anode mole fractions $x_{an,p}$ of hydrogen (H_2), nitrogen (N_2), and vapor (vap).
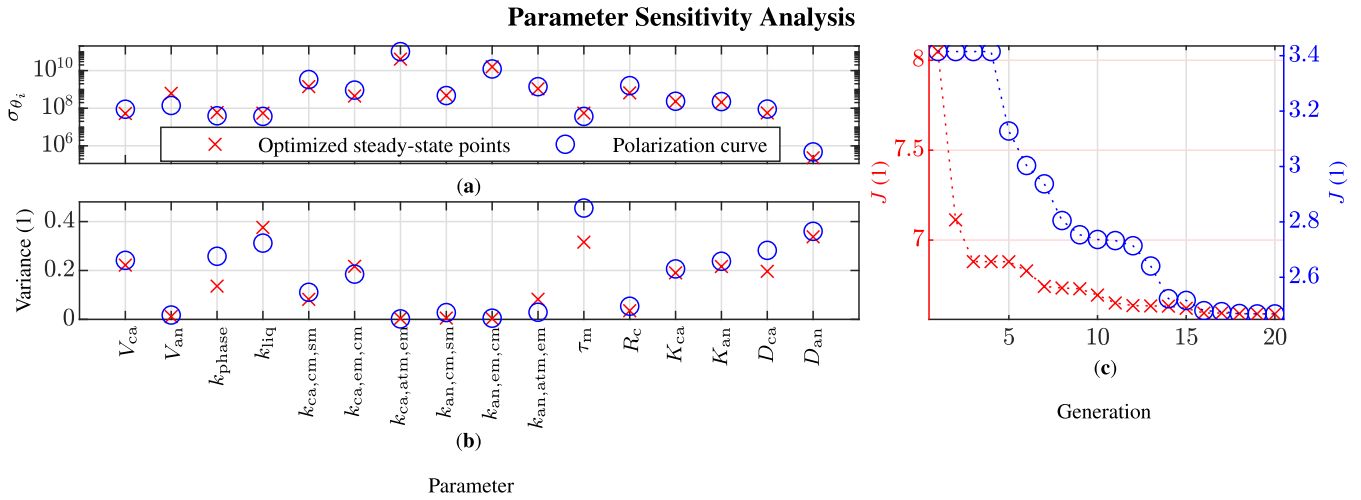
FIGURE 5. Plot (a) illustrates each parameter's total information σ_{θ_i} depending on the experiment. Higher values indicate better identifiability of the specific parameter. Plot (b) presents the obtained empirical variances of the parameters using the respective experiments, normalized with the squared parameter magnitudes, and lower variance means less parameter uncertainty. Plot (c) displays one of each experiment's parametrization objective value curves.

Fig. 5b shows the normalized empirical variances of the parameters, and lower values mean less parameter uncertainty. The variances correlate to the information content, as expected according to the Cramér-Rao inequality (3). A high information content means lower parameter variance, e.g., the cathode nozzle coefficient $k_{ca,atm,em}$, or vice versa, e.g., the anode combined diffusivity coefficient D_{an}. This property of the Fisher information helps make an a priori estimate on which parameters are well identifiable to simplify the optimization beforehand. In addition, it can be seen that the steady-state points experiment yield lower parameter variances for almost every parameter. A few exceptions include the liquid water removal coefficient k_{liq}, better identifiable in the polarization curve experiment. The latter operates more often with high loads (Fig. 4a,c), which provokes more liquid water generation and higher gas flows (Fig. 4d,f), which is ideal for removing liquid water. The high loads are also why the cathode $k_{ca,em,cm}$ and anode nozzle coefficient $k_{an,atm,em}$ have less uncertainty for the polarization curve experiment. This drawback of the steady-state points experiment can be balanced by extending the duration of high-load sections. Some parameters, such as the anode combined diffusivity coefficient D_{an}, are generally difficult to identify. The anode's diffusion is rarely a problem and might only be relevant during exceptionally high loads. Those operating regions are not allowed during the experiments to avoid FC degradation, leading to the named parameter's moderate identifiability. One of the many parametrization objective value (13) curves for each experiment is shown in Fig. 5c. The divergent magnitudes of the experiment's objective function are due to experiment-specific weightings, considering varying signal mean values, which does not automatically mean a worse fit of one. Considering all the available curves, the objective value for the steady-state points experiment converges faster in addition to the lower empirical variances, which

shows the beneficial impact of designing the experiments appropriately.

All experiments shown in Fig. 4 with their full length are utilized for the actual parametrization process to exploit all the available information. The combined parameter sensitivity analysis for all three experiments demonstrates that the anode combined diffusivity coefficient D_{an} and membrane time constant τ_m are poorly identifiable, similarly to Fig. 5a, so these two parameters are excluded from the optimization and kept constant at their initial value. The resulting parametrization objective value curve is qualitatively similar to those in Fig. 5c. In the interests of concision, the remainder of this paper only describes the chirp experiment. The latter covers the entire current operating range and frequency, so the dynamics of the remaining experiments are mostly covered. The parameterized model delivers the signals shown in Fig. 6.

Fig. 6a-e depict model outputs, Fig. 6f internal model concentrations; note that a validation data set is used here, which is not utilized during parametrization. The dashed lines are the measured references, and the solid lines are the simulated signals. The model outputs are very well-replicated, also indicated with scatter index S values at the second decimal place. The model voltage U has some deviations during the slow dynamics at the beginning and the lower peaks, as shown in Fig. 6a. The slowly decaying deviations at the beginning might be a consequence of the not ideal initialization of the simulation. The differences at the lower peaks are likely due to simplified modeling assumptions in the electrochemical model. The diffusion is modeled assuming steady-state, an especially rough approximation during high dynamic loads at the lower peaks. Also, the anode exit manifold pressure $p_{an,em}$ has a slight offset (Fig. 6e) due to simplifying assumptions in the recirculation flow modeling [16]. The remaining output signals (Fig. 6b,c,d), in essence, overlap

Parametrization
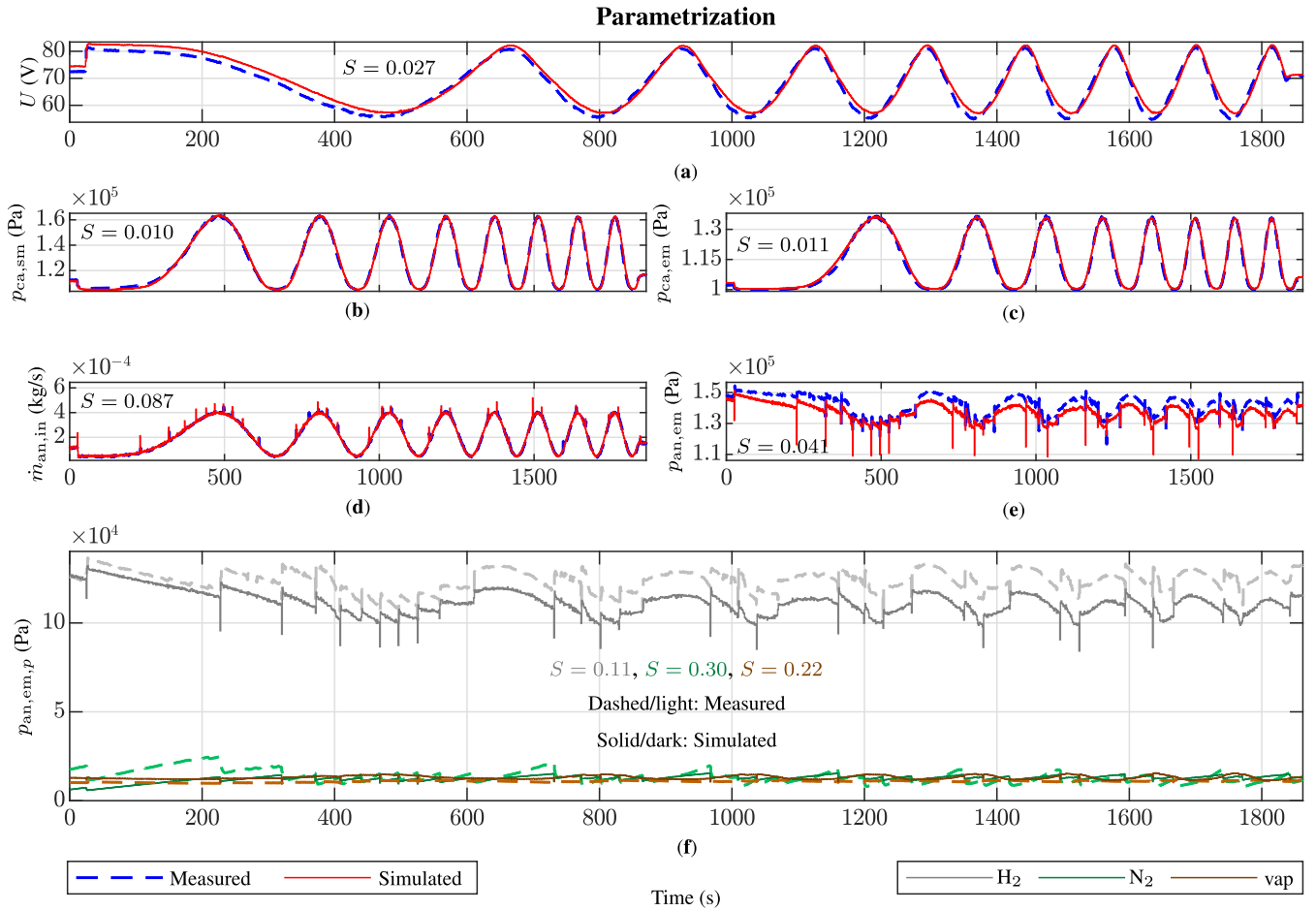
FIGURE 6. Model outputs: stack voltage U (Plot a), cathode supply $p_{ca,sm}$ (Plot b) and exit manifold pressure $p_{ca,em}$ (Plot c), and anode inflowing mass $\dot{m}_{an,in}$ (Plot d) and exit manifold pressure $p_{an,em}$ (Plot e). Plot (f) displays the internal anode exit manifold partial pressures $p_{an,em,p}$ for hydrogen (H_2), nitrogen (N_2), and vapor (vap), and the corresponding scatter index S is given in each plot. Dashed lines represent measured references, and solid ones the simulated signals.

with the measured references. The mass spectrometer measures the gaseous anode species mole fractions at the outlet, but the model delivers the species averaged for the whole stack due to the modeling assumptions. Thus, the individual species partial pressures $p_{an,em,p}$ for $p \in \{H_2, N_2, vap\}$ in the exit manifold are fitted during parametrization instead of the averaged model mole fractions to obtain a better agreement. The anode partial pressures $p_{an,em,p} = p_{an,em}x_{an,p}$ are easily obtained by multiplying the exit manifold pressure $p_{an,em}$ with the respective mole fractions $x_{an,p}$. The latter signals are all measured, and Fig. 6f illustrates the simulated and measured partial pressures. The signals are qualitatively and quantitatively well-replicated, but there are still some deviations and offsets, leading to higher S values for the partial pressures than for the model outputs. There are three main reasons for this: First, the mass spectrometer has an accumulated measurement tolerance of up to 5%. Second, the device does not differentiate between liquid and gaseous water. Third, as described, the model used simulates the averaged species for the whole stack while the measured species are diverted at the outlet to the measurement device. For

these reasons, the species replication errors are less weighted during the parametrization procedure.

D. EXPERIMENTAL OBSERVER VALIDATION
For validation, Fig. 7 (same validation data as in Fig. 6) shows the signals delivered by the observer: the corrected model outputs (Fig. 7a-e) and estimated internal gaseous anode partial pressures (Fig. 7f). The observer estimates the internal partial pressures by utilizing only the parameterized model (1), the measured model inputs u^*, and outputs y^*. The measured internal partial pressures are only depicted for reference and are entirely unknown to the observer.

Compared to the open-loop simulation in Fig. 6, the observer uses the measured outputs' feedback to improve the state estimations. The scatter index S improved significantly for hydrogen in Fig. 7f, which is also visually recognizable. Compared to the open-loop simulation in Fig. 6f, not only is the signal's qualitative behavior caught, but also its magnitude. The estimated nitrogen partial pressure by the observer deviates more than in the open-loop case with a
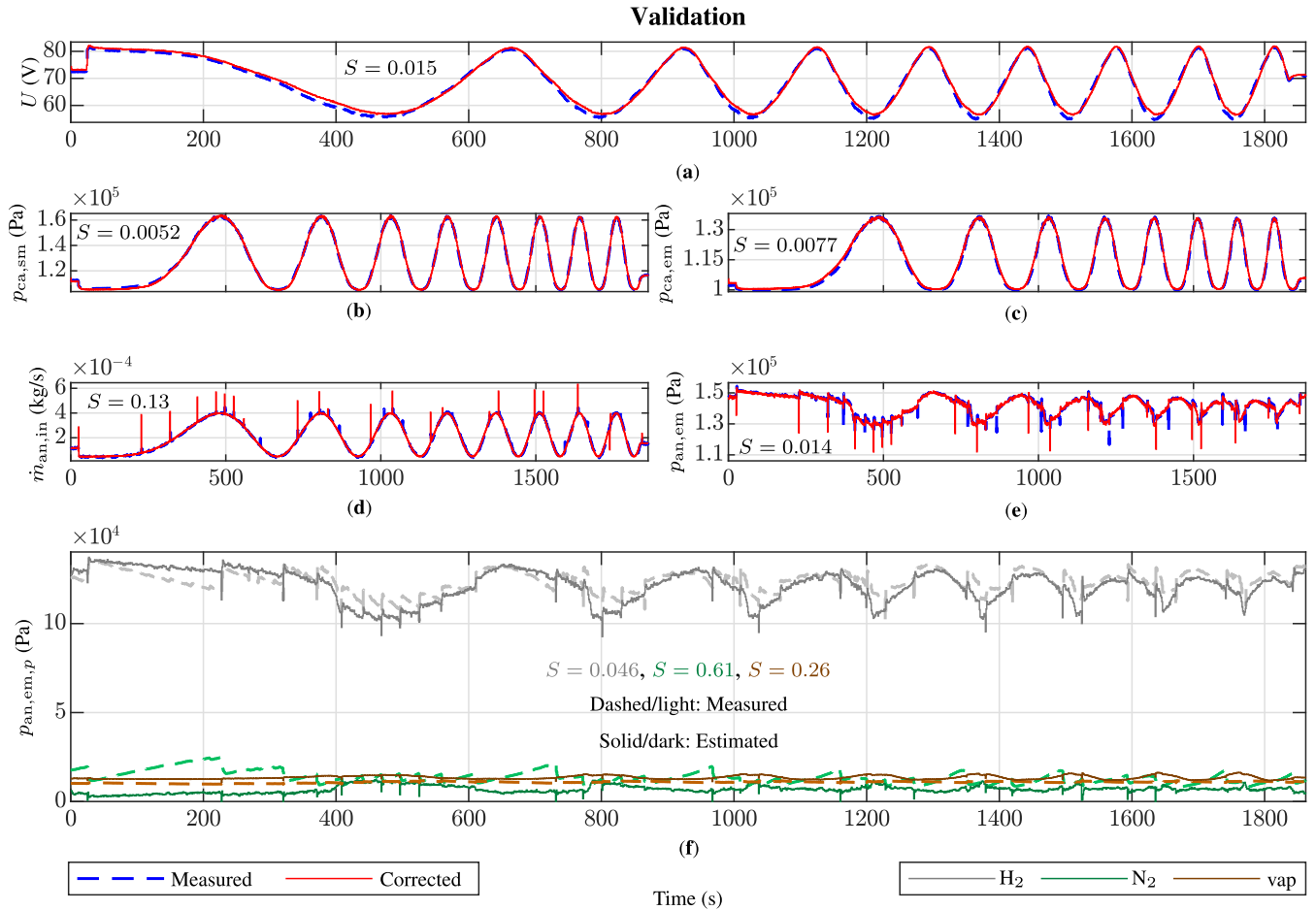
FIGURE 7. Model outputs: stack voltage U (Plot a), cathode supply $p_{ca,sm}$ (Plot b) and exit manifold pressure $p_{ca,em}$ (Plot c), and anode inflowing mass $\dot{m}_{an,in}$ (Plot d) and exit manifold pressure $p_{an,em}$ (Plot e). Plot (f) displays the internal anode exit manifold partial pressures $p_{an,em,p}$ for hydrogen (H_2), nitrogen (N_2), and vapor (vap), and the corresponding scatter index S is given in each plot. Dashed lines represent measured references, and solid ones the observer signals.

corresponding higher S value, which also applies to the vapor partial pressure, but on a smaller scale. The main reasons for this have already been mentioned: measurement tolerance, water phase differentiation, and spatial model assumptions. In particular, the measuring at the outlet is visually clearly noticeable for nitrogen. The measured nitrogen partial pressure accumulates at the outlet (the rising ramps are well visible) and is always higher than the estimated averaged values by the observer for the whole stack. However, it is considered that the estimations by the observer better represent the stack as a whole, and using the estimated states, the so-called corrected model outputs by the observer (Fig. 7a-e) yield scatter indices which are always lower than for the simulated signals in Fig. 6. The only exception is the anode inflowing mass $\dot{m}_{an,in}$ (Fig. 7d). This has a higher S value in the observer case caused by a more divergent correction of the signal spikes during the purging process. The reason is that purging is highly nonlinear, but the observer algorithm uses locally linearized Jacobians. Furthermore, to a large extent, the observer corrects the mentioned stack voltage U deviations due to improper initialization (Fig. 6a and Fig. 7a), and the offset in the anode exit manifold pressure $p_{an,em,p}$

(Fig. 6e) is also adjusted by the observer (Fig. 7e). The observer achieves both corrections by driving the internal states to more realistic configurations based on the feedback of the measured outputs. The improved scatter indices for the model outputs demonstrate that the estimated concentrations represent the whole stack better than the open-loop simulation counterparts, despite having higher S values for nitrogen and vapor. An explanation for the simulation model's behavior is that it is parametrized to measurements at the exit manifold, explaining why it mimics the behavior there instead of the averaged ones for the whole stack. Essentially, the model was parametrized to behave differently, which the observer corrects. Still, the estimated states by the observer coincide quantitatively and qualitatively well with the measurements, validating the observer itself. In conclusion, considering the reasons given above for deviation and the simple model, the observer's performance is outstanding.

For comparison, Fig. 8 shows the anode nitrogen partial pressure p_{an,em,N_2} estimated by a Kalman filter (KF), an extended KF (EKF), a CEKF [4], and a constrained unscented KF (CUKF) [33]. The KF is a linear estimation algorithm, EKF is the nonlinear version, the CEKF addi-

Observer Comparison
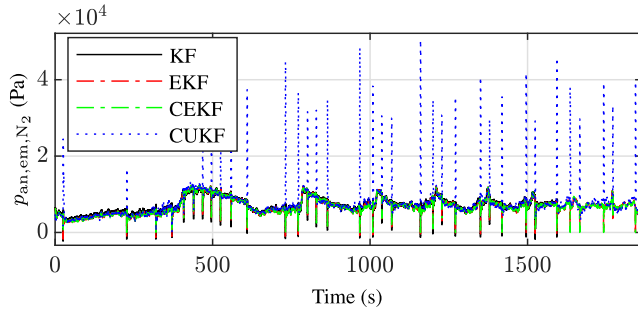
FIGURE 8. Comparison of anode nitrogen partial pressure p_{an,em,N_2} estimated by a Kalman filter (KF), an extended KF (EKF), a constrained EKF (CEKF), and a constrained unscented KF (UKF).

TABLE 2. Performance indices comparison between a Kalman filter (KF), an extended KF (EKF), a constrained EKF (CEKF), and a constrained unscented KF (UKF).

Scatter index S for	KF	EKF	CEKF	CUKF
U	0.015	0.015	0.015	0.018
$p_{ca,sm}$	0.0054	0.0052	0.0052	0.012
$p_{ca,em}$	0.0074	0.0077	0.0077	0.014
$\dot{m}_{an,in}$	0.13	0.13	0.13	0.086
$p_{an,em}$	0.015	0.014	0.014	0.029
p_{an,em,H_2}	0.045	0.046	0.046	0.079
p_{an,em,N_2}	0.59	0.61	0.61	0.63
$p_{an,em,vap}$	0.25	0.26	0.26	0.25
Relative computation time	0.28	0.99	1	4.7

tionally considers constraints, and the CUKF utilizes an unscented transformation, which does not require the model's Jacobians. Visually, all observers yield similar estimations, and only the CUKF has some big spikes during purging, which the others do not have. The reason could be that purging is a highly nonlinear process, and due to the required state sample points by the algorithm, minor changes in the states have a significant impact on the estimation. Quantitative performance indices for each observer are given in Table 2. These are the scatter index S between each observer signal and the measured counterpart and the computation time relative to the CEKF. The scatter indices show that all observers have a similar estimation performance, and the latter heavily depends on the tuning. Some are better for specific signals and others for others, and no single one is superior. What is more apparent is that constraints are strictly necessary to obtain physically meaningful results, e.g., the pressure gets negative during purging for the KF and EKF in Fig. 8. The UKF is too computationally expensive for control applications because it needs 4.7 times longer to calculate than the CEKF while not yielding superior performance. A constrained KF would be a reasonable compromise regarding performance and computation time, but the model's Jacobians are already calculated in a closed-loop setup for a model-based controller [17], which requires them for the strong nonlinearities (e.g., water phase change and droplet

removal). The CEKF uses the precalculated Jacobians in this constellation and does not require additional computation, significantly lowering the computational demand for the CEKF itself and enabling it to consider the nonlinearities better. In summary, the CEKF is a reasonable compromise for a control setup regarding estimation performance and computational requirements.

E. REMARKS ON WORKFLOW IMPLEMENTATION

The proposed design workflow is a holistic guideline for real-world observer implementations for FC concentrations. So that the workflow can play out its advantages, certain issues have to be considered. The presented methodologies require an appropriate system model because the DOE, parameter sensitivity analysis, and observer design are model-based. In addition, the model has to fulfill two conditions: identifiability and observability (please refer to the literature for the definitions). The identifiability also depends on the experiments, but the model should have a manageable number of parameters and a sophisticated structure to ensure a good starting point for parametrization. Observability is also not solely model dependent because the available physical sensors are decisive, but a good model structure is a sound basis for observing desired quantities. One key aspect of the workflow is the DOE, which implies the possibility of conducting experiments on the system. In many observer design cases, experiment execution is impossible, and the user must rely on existing measurements. Regarding observability, as already mentioned, the system must have the right equipment, e.g., sensors in advantageous positions. Moreover, suitable devices are necessary, e.g., a concentration measurement device to parametrize and validate the observer. Special measurement devices may not be necessary permanently during operation because one purpose of observers is to replace physical sensors and devices. If some criteria are not met, it does not automatically mean that this workflow is not applicable. The workflow can be used as an idea provider to create or adapt a system model, adjust the system, or include new sensors. The presented workflow is a guideline for implementation, but it is not inflexible and can, in fact, be adapted to the circumstances and possibilities of the specific use case.

IV. CONCLUSION

Observers are an effective method of obtaining unmeasured or even unmeasurable quantities with an estimation algorithm and measured quantities. In our study, an FC concentration observer was designed, and the estimated hydrogen, nitrogen, and water concentrations by the observer on the anode side were experimentally validated. The knowledge of the concentrations is necessary for diagnosis, degradation avoidance, and model-based control. A novel holistic observer design workflow was presented, covering the following methods for the first time: a model-based DOE was conducted to increase the experiment's model parameter sensitivity and input excitation range for improved identification and validation. The

experiments were executed on a 30 kW PEMFC system, and a key component of our approach is the mass spectrometer utilized to obtain concentration measurements. A model parameter sensitivity analysis was performed based on the available measurements to identify poorly identifiable parameters. These were excluded in the subsequent nonlinear identification in order to simplify it. Finally, based on the CEKF estimation algorithm, an FC concentration observer was designed and experimentally validated. The presented workflow is demonstrated based on a control-oriented PEMFC stack model, and the model-based DOE and the experimental validation with a mass spectrometer, including dynamic operation, are unique in the literature for PEMFC observers. In addition, the obtained results were discussed in detail, and the validated observer delivered an outstanding concentration estimation performance. Ultimately, the observer is ready for real-world applications such as online diagnosis and model-based control.

Further research topics would include investigating the observer's online diagnosis capabilities and behavior in a closed-loop setting via simulation followed by experimental studies. In order to improve the DOE, an online capable DOE controller could be developed, which optimizes the parameter identifiability online during experiment execution. This controller could consider unavoidable control errors and dynamically excite the system, favorable for time constant-like parameters.

APPENDIX
ABBREVIATIONS
The following abbreviations are used in this manuscript:

CEKF	Constrained extended Kalman filter.
CUKF	Constrained unscented Kalman filter.
DOE	Design of Experiments.
EKF	Extended Kalman filter.
FC	Fuel cell.
FIM	Fisher information matrix.
KF	Kalman filter.
PEMFC	Polymer electrolyte membrane fuel cell.

NOMENCLATURE
The following abbreviations are used in this manuscript:

SUBSCRIPTS
0	Initial.
θ	Parameter.
θ_{ms}	Most significant parameter.
e	Prediction error.
u	Input.
x	State, or process noise.
x_0	Initial state.
y	Output, or measurement noise.
$\hat{x}$	State estimate.
an	Anode.

atm	Atmosphere.
ca	Cathode.
cm	Center manifold.
c	Contact.
em	Exit manifold.
H_2	Hydrogen.
in	Inflow.
lim	Limit.
liq	Liquid water.
max	Maximum.
min	Minimum.
ms	Most significant.
m	Membrane.
N_2	Nitrogen.
nrm	Normalized.
O_2	Oxygen.
opt	Optimized.
phase	Phase change.
reci	Recirculation.
sm	Supply manifold.
vap	Vapor.
θ_i	Parameter i.
i	Parameter running index.
j	Singular value running index.
k	Sampling instant.
l	Input running index.
m	State running index.
n_θ	Number of parameters.
p	Mole fraction running index.

SYMBOLS
α	Valve position in 1.
$\boldsymbol{\Lambda}$	Lagrange multiplier vector $\mathbb{R}^9$ ($\mathbb{R}^{n_x}$).
$\boldsymbol{\psi}$	Output parameter sensitivity vector $\mathbb{R}^5$ ($\mathbb{R}^{n_y}$).
$\boldsymbol{\psi}$	Output parameter sensitivity vector $\mathbb{R}^5$ ($\mathbb{R}^{n_y}$).
$\boldsymbol{\Sigma}$	Covariance matrix $\mathbb{R}^{5\times5}$, or $\mathbb{R}^{9\times9}$ ($\mathbb{R}^{n_y\times n_y}$, or $\mathbb{R}^{n_x\times n_x}$).
$\boldsymbol{\theta}$	Vector containing the tunable parameters $\mathbb{R}^{16}$ ($\mathbb{R}^{n_\theta}$).
$\boldsymbol{\xi}$	State parameter sensitivity vector $\mathbb{R}^9$ ($\mathbb{R}^{n_x}$).
$\boldsymbol{A}$	System matrix $\mathbb{R}^{9\times9}$ ($\mathbb{R}^{n_x\times n_x}$).
$\boldsymbol{C}$	Output matrix $\mathbb{R}^{5\times9}$.
$\boldsymbol{F}$	System prediction function $\mathbb{R}^9$ ($\mathbb{R}^{n_x}$).
$\boldsymbol{f}$	System function $\mathbb{R}^9$ ($\mathbb{R}^{n_x}$).
$\boldsymbol{g}$	Output function $\mathbb{R}^5(\mathbb{R}^{n_y})$.
$\boldsymbol{H}$	Matrix for Kalman gain calculation $\mathbb{R}^{5\times5}$ ($\mathbb{R}^{n_y\times n_y}$).
$\boldsymbol{I}$	Identity matrix $\mathbb{R}^{9\times9}$ ($\mathbb{R}^{n_x\times n_x}$).
$\boldsymbol{K}$	Matrix for Kalman gain calculation $\mathbb{R}^{9\times5}$ ($\mathbb{R}^{n_x\times n_y}$).
$\boldsymbol{L}$	Optimal Kalman gain matrix $\mathbb{R}^{9\times5}$ ($\mathbb{R}^{n_x\times n_y}$).
$\boldsymbol{M}$	Fisher information matrix $\mathbb{R}^{n_\theta\times n_\theta}$.
$\boldsymbol{Q}$	Weighting, or regularization matrix $\mathbb{R}^{5\times5}$ ($\mathbb{R}^{n_y\times n_y}$), or $\mathbb{R}^{n_\theta\times n_\theta}$.
$\boldsymbol{S}$	Singular value matrix $\mathbb{R}^{n_\theta\times n_\theta}$.

U	Left singular vector matrix $\mathbb{R}^{n_\theta \times n_\theta}$.
u	Input vector $\mathbb{R}^{10}$ ($\mathbb{R}^{n_u}$).
u^*	Measured input vector $\mathbb{R}^{10}$ ($\mathbb{R}^{n_u}$).
V	Right singular vector matrix $\mathbb{R}^{n_\theta \times n_\theta}$.
v	Right singular vector $\mathbb{R}^{n_\theta}$.
w	Noise vector $\mathbb{R}^5$, or $\mathbb{R}^9$ ($\mathbb{R}^{n_y}$, or $\mathbb{R}^{n_x}$).
x	State vector $\mathbb{R}^9$ ($\mathbb{R}^{n_x}$).
x^*	Noisy (and measured) state vector $\mathbb{R}^9$ ($\mathbb{R}^{n_x}$).
y	Output vector $\mathbb{R}^5$ ($\mathbb{R}^{n_y}$).
y^*	Noisy (and measured) output vector $\mathbb{R}^5$ ($\mathbb{R}^{n_y}$).
γ	Threshold in 1.
$\hat{\Sigma}$	Updated covariance estimate matrix $\mathbb{R}^{9 \times 9}$ ($\mathbb{R}^{n_x \times n_x}$).
$\hat{\Sigma}^-$	Predicted covariance estimate matrix $\mathbb{R}^{9 \times 9}$ ($\mathbb{R}^{n_x \times n_x}$).
$\hat{x}$	Updated state estimate vector $\mathbb{R}^9$ ($\mathbb{R}^{n_x}$).
$\hat{x}^-$	Predicted state estimate vector $\mathbb{R}^9$ ($\mathbb{R}^{n_x}$).
$\hat{y}$	Updated output estimate vector $\mathbb{R}^5$ ($\mathbb{R}^{n_y}$).
$\hat{y}^-$	Predicted output estimate vector $\mathbb{R}^5$ ($\mathbb{R}^{n_y}$).
$\hat{y}$	Estimated (or simulated) signal $\mathbb{R}^{1 \times 1}$.
λ	Stoichiometry in 1.
$\mathcal{N}$	Normal distribution.
$\bar{x}$	Expected value of state vector $\mathbb{R}^9$ ($\mathbb{R}^{n_x}$).
σ	Singular value, or total information of a parameter.
τ	Time constant in s.
θ	Parameter.
$\tilde{L}$	Adjusted optimal Kalman gain matrix $\mathbb{R}^{9 \times 5}$ ($\mathbb{R}^{n_x \times n_y}$).
$\tilde{x}$	Clipped state estimate vector $\mathbb{R}^9$ ($\mathbb{R}^{n_x}$).
φ	Relative humidity in 1.
a	Water activity in 1.
D	Combined diffusivity parameter in mol/s.
I	Current in A.
J	Objective function $\mathbb{R}^{1 \times 1}$.
K	Intrinsic exchange current parameter in A/m^2.
k	Nozzle, or mass flow coefficient in kg/(s $\cdot$ Pa), m^2, or 1/s.
M	Fisher information for a single parameter $\mathbb{R}^{1 \times 1}$.
m	Mass in kg.
n	Number in 1.
P	Power in W.
p	Pressure in Pa.
R	Ohmic resistance in Ω.
S	Scatter index, or normalized root-mean-square error in 1.
T	Fuel cell temperature in K.
t	Time in s.
U	Voltage in V.
u	Input.
V	Volume in m^3.

v	Right singular vector component.
x	Gaseous species mole fraction in 1.
y^*	Measured signal $\mathbb{R}^{1 \times 1}$.

REFERENCES

[1] Y. Wang, K. S. Chen, J. Mishler, S. C. Cho, and X. C. Adroher, "A review of polymer electrolyte membrane fuel cells: Technology, applications, and needs on fundamental research," *Appl. Energy*, vol. 88, no. 4, pp. 981–1007, 2011. [Online]. Available: https://linkinghub.elsevier.com/retrieve/pii/S0306261910003958

[2] H. Yuan, H. Dai, X. Wei, and P. Ming, "Model-based observers for internal states estimation and control of proton exchange membrane fuel cell system: A review," *J. Power Sources*, vol. 468, Aug. 2020, Art. no. 228376. [Online]. Available: https://linkinghub.elsevier.com/retrieve/pii/S0378775320306807

[3] M. Vrlić, D. Ritzberger, and S. Jakubek, "Safe and efficient polymer electrolyte membrane fuel cell control using successive linearization based model predictive control validated on real vehicle data," *Energies*, vol. 13, no. 20, p. 5353, Oct. 2020. [Online]. Available: https://www.mdpi.com/1996-1073/13/20/5353

[4] L. Böhler, D. Ritzberger, C. Hametner, and S. Jakubek, "Constrained extended Kalman filter design and application for on-line state estimation of high-order polymer electrolyte membrane fuel cell systems," *Int. J. Hydrogen Energy*, vol. 46, no. 35, pp. 18604–18614, May 2021. [Online]. Available: https://linkinghub.elsevier.com/retrieve/pii/S0360319921008351

[5] S. de Lira, V. Puig, J. Quevedo, and A. Husar, "LPV observer design for PEM fuel cell system: Application to fault detection," *J. Power Sources*, vol. 196, no. 9, pp. 4298–4305, May 2011. [Online]. Available: https://linkinghub.elsevier.com/retrieve/pii/S0378775310020756

[6] M. Piffard, M. Gerard, R. D. Fonseca, P. Massioni, and E. Bideaux, "Sliding mode observer for proton exchange membrane fuel cell: Automotive application," *J. Power Sources*, vol. 388, pp. 71–77, Jun. 2018. [Online]. Available: https://linkinghub.elsevier.com/retrieve/pii/S0378775318302994

[7] L. Xu, J. Hu, S. Cheng, C. Fang, J. Li, M. Ouyang, and W. Lehnert, "Nonlinear observation of internal states of fuel cell cathode utilizing a high-order sliding-mode algorithm," *J. Power Sources*, vol. 356, pp. 56–71, Jul. 2017. [Online]. Available: https://linkinghub.elsevier.com/retrieve/pii/S0378775317305633

[8] H. Görgün, M. Arcak, and F. Barbir, "An algorithm for estimation of membrane water content in PEM fuel cells," *J. Power Sources*, vol. 157, no. 1, pp. 389–394, Jun. 2006. [Online]. Available: https://linkinghub.elsevier.com/retrieve/pii/S0378775305009857

[9] J. Liu, S. Laghrouche, F.-S. Ahmed, and M. Wack, "PEM fuel cell air-feed system observer design for automotive applications: An adaptive numerical differentiation approach," *Int. J. Hydrogen Energy*, vol. 39, no. 30, pp. 17210–17221, Oct. 2014. [Online]. Available: https://linkinghub.elsevier.com/retrieve/pii/S036031991402271X

[10] M. Benallouch, R. Outbib, M. Boutayeb, and E. Laroche, "A new scheme on robust unknown input nonlinear observer for PEM fuel cell stack system," in *Proc. IEEE Int. Conf. Control Appl.*, New York, NY, USA, Jul. 2009, pp. 613–618. [Online]. Available: http://ieeexplore.ieee.org/document/5280955/

[11] D. Rotondo, R. M. Fernandez-Canti, S. Tornil-Sin, J. Blesa, and V. Puig, "Robust fault diagnosis of proton exchange membrane fuel cells using a Takagi–Sugeno interval observer approach," *Int. J. Hydrogen Energy*, vol. 41, no. 4, pp. 2875–2886, Jan. 2016. [Online]. Available: https://linkinghub.elsevier.com/retrieve/pii/S0360319915301166

[12] H. Yuan, H. Dai, X. Wei, and P. Ming, "A novel model-based internal state observer of a fuel cell system for electric vehicles using improved Kalman filter approach," *Appl. Energy*, vol. 268, Jun. 2020, Art. no. 115009. [Online]. Available: https://linkinghub.elsevier.com/retrieve/pii/S0306261920305213

[13] M. Haschka, T. Weickert, and V. Krebs, "Application of a sigma-point Kalman-Filter for the online estimation of fractional order impedance models for solid oxide fuel cells," *IFAC Proc. Volumes*, vol. 39, no. 11, pp. 194–199, Jan. 2006. [Online]. Available: https://linkinghub.elsevier.com/retrieve/pii/S1474667015364983

[14] K. Chen, S. Laghrouche, and A. Djerdir, "Fuel cell health prognosis using unscented Kalman filter: Postal fuel cell electric vehicles case study," *Int. J. Hydrogen Energ.*, vol. 44, no. 3, pp. 1930–1939, Jan. 2019. [Online]. Available: https://linkinghub.elsevier.com/retrieve/pii/S0360319918337029

[15] J. Liu, W. Luo, X. Yang, and L. Wu, "Robust model-based fault diagnosis for PEM fuel cell air-feed system," *IEEE Trans. Ind. Electron.*, vol. 63, no. 5, pp. 3261–3270, May 2016. [Online]. Available: http://ieeexplore.ieee.org/document/7420651/

[16] Z. P. Du, A. Kravos, C. Steindl, T. Katrašnik, S. Jakubek, and C. Hametner, "Physically motivated water modeling in control-oriented polymer electrolyte membrane fuel cell stack models," *Energies*, vol. 14, no. 22, p. 7693, Nov. 2021. [Online]. Available: https://www.mdpi.com/1996-1073/14/22/7693

[17] M. Vrlić, D. Ritzberger, and S. Jakubek, "Model-predictive-control-based reference governor for fuel cells in automotive application compared with performance from a real vehicle," *Energies*, vol. 14, no. 8, p. 2206, Apr. 2021. [Online]. Available: https://www.mdpi.com/1996-1073/14/8/2206

[18] H. Nijmeijer and A. van der Schaft, "Introduction," in *Nonlinear Dynamical Control Systems*. New York, NY, USA: Springer, 1990, pp. 1–22. [Online]. Available: http://link.springer.com/10.1007/978-1-4757-2101-0

[19] L. Ljung, "Parameter estimation methods," in *System Identification: Theory for the User*, 2nd ed. Englewood Cliffs, NJ, USA: Prentice-Hall, 1999, pp. 169–207.

[20] H. Cramér, *Mathematical Methods of Statistics*, vol. 9. Princeton, NJ, USA: Princeton Univ. Press, 1999.

[21] Z. P. Du, C. Steindl, and S. Jakubek, "Efficient two-step parametrization of a control-oriented zero-dimensional polymer electrolyte membrane fuel cell model based on measured stack data," *Processes*, vol. 9, no. 4, p. 713, Apr. 2021. [Online]. Available: https://www.mdpi.com/2227-9717/9/4/713

[22] *MathWorks Find Minimum of Function Using Genetic Algorithm—MATLAB Ga*. Accessed: Feb. 15, 2021. [Online]. Available: https://www.mathworks.com/help/gads/ga.html

[23] D. H. von Seggern, "Transcendental functions," in *CRC Standard Curves and Surfaces with Mathematica*. New York, NY, USA: Chapman & Hall/CRC, May 2016, pp. 97–192. [Online]. Available: https://www.taylorfrancis.com/books/9781315372570

[24] *V&F Analyse–und Messtechnik GmbH, Product Flyer PEMSense*. Accessed: Aug. 9, 2022. [Online]. Available: https://www.vandf.com/en/service/documents/product-flyer/vf-analyzers/?no_cache=1&download=Product_Flyer_PEMSense_2020_November.pdf

[25] J. F. M. Van Doren, S. G. Douma, P. M. J. Van den Hof, J. D. Jansen, and O. H. Bosgra, "Identifiability: From qualitative analysis to model structure approximation," *IFAC Proc. Volumes*, vol. 42, no. 10, pp. 664–669, 2009. [Online]. Available: https://linkinghub.elsevier.com/retrieve/pii/S1474667016387249

[26] J. D. Stigter and J. Molenaar, "A fast algorithm to assess local structural identifiability," *Automatica*, vol. 58, pp. 118–124, Aug. 2015. [Online]. Available: https://linkinghub.elsevier.com/retrieve/pii/S0005109815001946

[27] C. L. C. Diana, T. Barz, S. Körkel, and G. Wozny, "Nonlinear ill-posed problem analysis in model-based parameter estimation and experimental design," *Comput. Chem. Eng.*, vol. 77, pp. 24–42, Jun. 2015. [Online]. Available: https://linkinghub.elsevier.com/retrieve/pii/S0098135415000733

[28] D. Ritzberger, J. Höflinger, Z. P. Du, C. Hametner, and S. Jakubek, "Data-driven parameterization of polymer electrolyte membrane fuel cell models via simultaneous local linear structured state space identification," *Int. J. Hydrogen Energy*, vol. 46, no. 21, pp. 11878–11893, Mar. 2021. [Online]. Available: https://linkinghub.elsevier.com/retrieve/pii/S0360319921000951

[29] M. P. Eckert, G. Buchsbaum, and A. B. Watson, "Separability of spatiotemporal spectra of image sequences," *IEEE Trans. Pattern Anal. Mach. Intell.*, vol. 14, no. 12, pp. 1210–1213, Dec. 1992. [Online]. Available: http://ieeexplore.ieee.org/document/177387/

[30] O. Nelles, "Introduction to optimization," in *Nonlinear System Identification*. Berlin, Germany: Springer, 2001, pp. 23–34. [Online]. Available: http://link.springer.com/10.1007/978-3-662-04323-3

[31] *MathWorks Symbolic Math Toolbox—MATLAB*. Accessed: Jan. 30, 2021. [Online]. Available: https://www.mathworks.com/products/symbolic.html

[32] L. Zambresky, "A verification study of the global WAM model," Eur. Centre Medium-Range Weather Forecasts, Reading, U.K., Tech. Rep. 63, 1989. Accessed: May 9, 2022. [Online]. Available: http://www.citeulike.org/group/11419/article/6355268

[33] R. Kandepu, L. Imsland, and B. A. Foss, "Constrained state estimation using the unscented Kalman filter," in *Proc. 16th Medit. Conf. Control Autom.*, New York, NY, USA, Jun. 2008, pp. 1453–1458. [Online]. Available: http://ieeexplore.ieee.org/document/4602001/

ZHANG PENG DU received the B.Sc. and Dipl.-Ing. (equivalent to M.Sc.) degrees in mechanical engineering (management) from TU Wien, Vienna, Austria, in 2018 and 2019, respectively.

Since 2020, he has been an University Assistant at the Institute of Mechanics and Mechatronics, TU Wien. His current research interests include nonlinear system identification, modeling, and optimization.

CHRISTOPH STEINDL received the B.Sc. and M.Sc. degrees in mechanical engineering from TU Wien, Vienna, Austria, in 2016 and 2019, respectively.

Since 2019, he has been an University Assistant at the Institute of Powertrains and Automotive Technology, TU Wien. His research interests include modeling, experimental investigation, and control of fuel cell hybrid propulsion systems.

STEFAN JAKUBEK received the M.Sc. degree in mechanical engineering, the Ph.D. degree in technical sciences, and the Habilitation (Professorial Qualification) degree in control theory and system dynamics from TU Wien, Vienna, Austria, in 1997, 2000, and 2007, respectively.

From 2006 to 2009, he was the Head of Development for Hybrid Powertrain Calibration and Battery Testing Technology, AVL List GmbH, Graz, Austria (automotive industry company). He is currently a Professor and the Head of the Institute of Mechanics and Mechatronics, TU Wien. His research interests include fault diagnosis, nonlinear system identification, and simulation technology.

CHRISTOPH HAMETNER received the M.Sc. degree in mechanical engineering, the Ph.D. degree in technical sciences, and the Habilitation (Professorial Qualification) degree in control theory and system dynamics from TU Wien, Vienna, Austria, in 2005, 2007, and 2014, respectively.

He is currently the Head of the Christian Doppler Laboratory for Innovative Control and Monitoring of Automotive Powertrain Systems, TU Wien. His research interests include nonlinear system identification, modeling, and control.

● ● ●